BEAM SHAPING BY OPTICAL MAP TRANSFORMS

Manisha Singh

Master Thesis

May 2012

Department of physics and mathematics
University of Eastern Finland

Manisha Singh *Beam shaping by optical map transform* , 55 pages
University of Eastern Finland
Msc. in Photonics
Instructors Prof. Jari Turunen
Docent Jani Tervo

Abstract

This work contains theoretical, numerical, and experimental studies on laser beam shaping. The basic concepts of wave optical analysis of propagation of optical fields and the scalar theory of diffraction are discussed, and applied to the design of diffractive beam shaping elements which transform a Gaussian beam into a uniform irradiance profile in the Fresnel domain or in far field. Fabrication and characterization of these elements is also considered. Conclusions are made on the choice of design, depending on the tolerances available.

Preface

My interest to become an optical designer in future led to my interest in diffractive optics which finally encouraged to this thesis. During these time I have experienced a lot from theory to its application. Many of these ideas originated as a result of brainstorming discussion in ACTMOST project.

I am really grateful to my supervisor, Prof. Jari Turunen and Docent Jani Tervo, who have guided me and shown their confidence in me. I will always be indebted to their constant help and for increasing a self confidence in me. I also want to thank Prof. Pasi Vahimaa, the head of our department and i would like to offer my special thanks to Faculty of Forestry and Sciences for providing financial support during my Masters studies.

This thesis would not have been possible without the co-operation and kind help of my supervisors, Janne Laukkanen, Pertti Pääkkönen, Tommi Itkonen, and members of technical and electrical workshop.

Finally, my warmest thanks goes to my parents and friends who have encouraged and supported me during these years.

Joensuu, May 2012
Manisha Singh

Contents

Chapter I

Introduction

Beam shaping started back in seventh century B.C with the use of magnifying glass to concentrate sunlight to burn wood [1]. For about 180 years, use of Fresnel lenses [2, 3] in light houses, traffic lights, wireless networks, and overhead projectors have been some of the important beam shaping applications. Beam shaping has been used for improving technologies like lithography [4], laser printing [5], some medicine and laboratory research [5], material processing [6], micro machining, laser processing [7], line integrator [8], camera optics [8], and holography [9].

Beam shaping methods can be divided in two groups. First, there are beam integrators in which the input beam is split into separate components and merged at target plane to get a desired profile [7]. The second approach to beam shaping, to be considered in this thesis, is based on geometrical map transforms. A beam transformer performs field mapping from input to target plane [10–12]. For example, transformation of Gaussian beam into top-hat [13], super-Gaussian, Bessel [14], Fermi-Dirac, or some other shape with specified irradiance [15] can be of interest. Beam transformers can be based on refractive [16], reflective or diffractive optics [17]. This thesis mainly focuses on diffractive optics.

One of the first beam-shaping papers was published by Frieden in 1965 [18] and a device using map-transform techniques was introduced by Han in 1983 [19]. It converted a Gaussian beam into a uniform irradiance distribution by use of two consecutive elements. Later, rotationally symmetric and one dimensional axicons [20–22] and beam-shaping elements for lasers [13, 23–29] were designed using a single element.

This thesis concerns the design, tolerance analysis, fabrication, and characteri-

zation of beam shaping elements based on geometrical map transforms. This work is partially theoretical and partially experimental. Chapter II deals with the scope of the thesis and chapter III deals with fundamentals of diffraction and scalar wave theory. In chapter IV, methods for analysis of propagation of optical fields are considered for uniform medium. The paraxial approximation case like Fresnel propagation formula and the complex amplitude transmittance approach method are also discussed. Chapter V deals with design examples and theoretical simulation results on diffractive beam shaping elements. Design, optimization, and tolerance analysis are discussed in chapter VI. Finally, conclusions are drawn in chapter VII and some prospects for future work are outlined in chapter VIII.

Chapter II

Aim and scope

Transforming a Gaussian beam to one with uniform irradiance is important for many applications: for example laser material processing, laser scanning, and laser radar [7] require uniform irradiance with desired shape and sharp edges. The beam properties at a given distance z from the initial plane are completely determined by the beam properties at the initial plane. Usually one is interested in the intensity distribution at a given target plane. Then the question arises: how can a desired intensity distribution in the plane z or at a some other surface be produced only by choosing the beam properties at the initial plane?

The aim of this thesis is to use diffractive optics to convert a known input field or beam into one with defined output distribution. In practise, the most important example is converting a Gaussian input beam to flat top beam. The approach adopted here is based on the geometrical map transform technique. The concept is old, but realization of the required diffractive elements at high light efficiency has become possible much more recently, as a result of developments in lithographic fabrication techniques of phase-modulating elements [36].

The beam shaping diffractive elements perform a 1-to-1 mapping of the input light to output profile, and we can control both intensity and phase of the output beam. Designing the phase function of beam shaping element is done using map transform method in Matlab.

Some critical factors like fabrication errors and alignment issues were considered as they affect the performance of these beam shaping elements.

Within scalar theory the desired complex amplitude transmittance function of the element may be calculated by propagating the field from the signal plane to the

element plane and dividing by the incident beam. The resulting element is then characterized by continuous amplitude and phase modulation. Usually one prefers phase only modulation, because it is easier to produce elements that modulate only the phase rather than the phase and amplitude. It is always possible to modulate both phase and amplitude by separately producing them as shown in Fig. 2.1. Desired amplitude and phase can be obtained with help of two element system. The first element maps the field in such a way that we get desired amplitude at second element, which then transforms the phase to correct form. Thus we have desired amplitude and phase at the target plane. But this thesis deals with phase modulation as amplitude modulation can lead to loss of laser energy and phase modulation can remap intensity in such a way that there is no loss. Two cases using single element

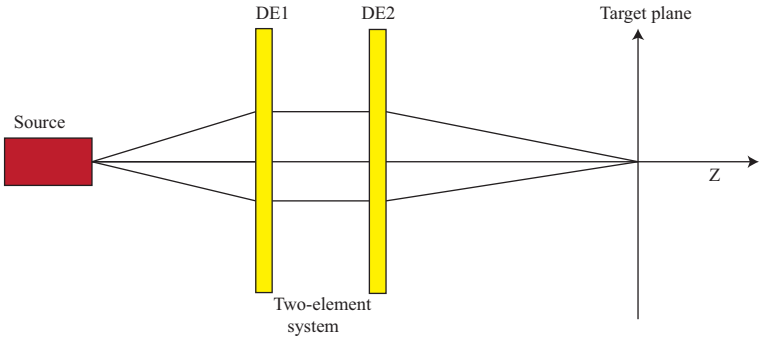

Figure 2.1: Transforming input light from the source to specified complex field distribution using two diffractive elements.

were dealt in this thesis :

1. Fresnel domain or paraxial approach

When the propagating wave travels close to z-axis or has very small divergence, the geometry is said to be *Paraxial*. Paraxial geometry has been used in many applications like laser scanning and laser processing [7]. One way of achieving beam transformation in Fresnel domain is to design a phase transform element which transforms the input Gaussian beam to desired flat-top profile as seen in Fig. 2.2. Here, He-Ne laser with stable mode is considered and a Gaussian beam with plane input wave front is taken into consideration.

2. Far-field case

In case of a target plane located in the far field, we can use the paraxial approxi-

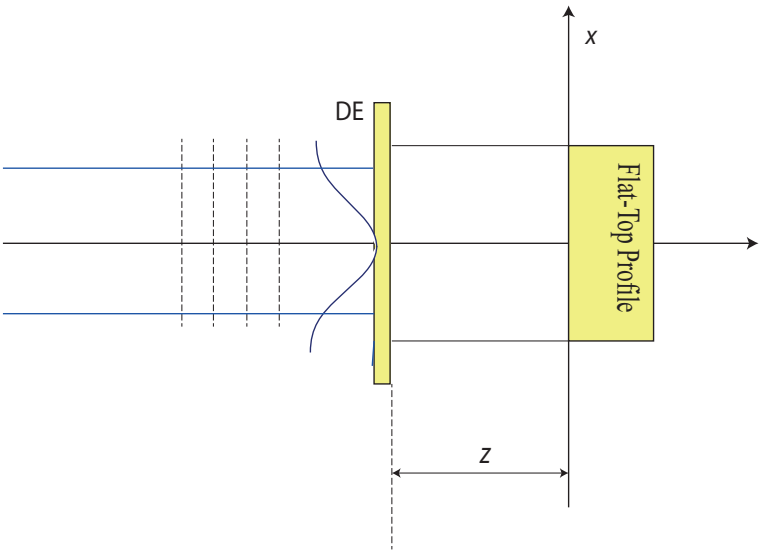

Figure 2.2: Map transformation of incident Gaussian beam to flat-top profile in Fresnel domain.

mation as long as the beam divergence is small. If the required divergence angle is large (tens of degrees), a non paraxial approach should be used like in the case of laser line generators. One beam shaping geometry to be considered in this thesis is illustrated in Fig. 2.3: here the laser emit a non-paraxial Gaussian and the cylindrical lens (CL) forms the image of the laser output face, and the distance between this image and the element $d \gg Z_{\mathrm{R}}$ (Rayleigh length) of the beam so that the field at the plane of the element has the radius of curvature R equals to d (far zone). Thus, in ray picture, we can treat the image of the laser as a point source. Map transformation between incident angle θ and fan angle Φ should convert the incident intensity profile into a flat top profile in far field (z tends to infinity) in frequency space. We get flat top profile over a plane surface as shown in Fig. 2.3.

In both paraxial and non-paraxial approach, a Gaussian beam is converted into exact flat-top and super Gaussian beam profile and wave optical analysis is done throughout.

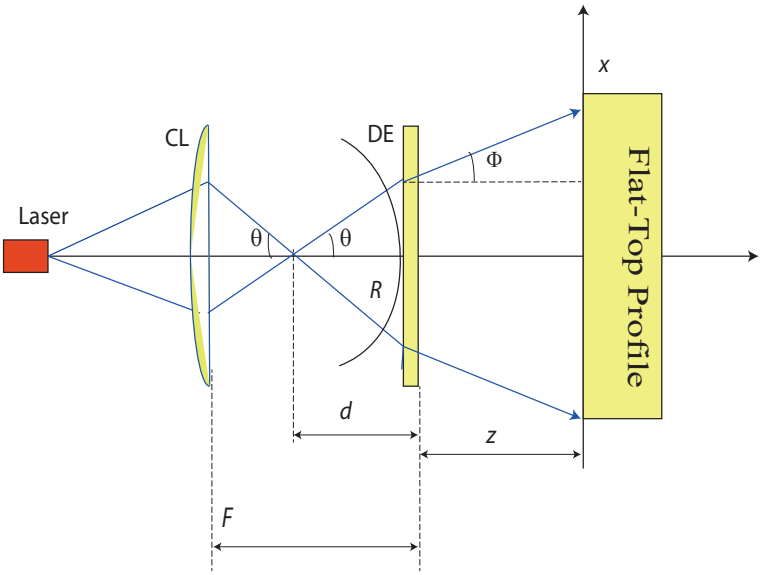

Figure 2.3: Map transformation of input divergence angle θ and output fan angle Φ , which converts incident Gaussian beam to flat-top profile in far field $z \to \infty$ in frequency space. Flat top profile is in plane surface.

Chapter III

Free-space propagation of optical fields

3.1 Introduction

Maxwell's equations [31] form the basis for considering propagation of any electromagnetic field. When we talk about wavelength scale feature size for diffractive element, an accurate analysis of the element requires that the light is treated as an electromagnetic wave. Here, however it sufficient to consider scalar theory of electromagnetic field which ignores polarization effects.

One characteristic of Maxwell's equations is that every Cartesian component $U(x, y, z)$ of the electric field in space-frequency domain obeys well known Helmholtz wave Eq.(3.1).

$$\nabla^2 U(x, y, z) + k^2 U(x, y, z) = 0, \tag{3.1}$$

where $k = 2\pi/\lambda$ is the wavenumber and λ is the wavelength of light. The simplest solution of Eq.(3.1)is a harmonic plane wave.

$$U(x, y, z) = U_o e^{i(k_x x + k_y y + k_z z)} \tag{3.2}$$

where U_o is complex constant, ω is the angular frequency of the wave, and $\mathbf{k} = (k_x, k_y, k_z)$ is the wave vector. Here stationary fields are taken into consideration, and hence we assume $|U|$ is time independent.

3.2 Angular spectrum representation

The angular spectrum representation is a mathematical technique to describe how the field propagates over a certain distance. Here we consider propagation in free

space. The approach is to calculate the Fourier transform of the Helmholtz Eq.(3.1) with respect to x and y yielding

$$\frac{d^2}{dz^2}\widetilde{U}(u,v,z) + 4\pi^2\beta^2\widetilde{U}(u,v,z) = 0, \tag{3.3}$$

where

$$\beta^2 = \left(\frac{k}{2\pi}\right)^2 - (u^2+v^2) \tag{3.4}$$

and the Fourier transform is defined here as

$$\widetilde{U}(u,v,z) = \left(\frac{1}{2\pi}\right)^2 \iint_{-\infty}^{\infty} U(x,y,z)e^{-i2\pi(ux+vy)}dxdy. \tag{3.5}$$

The general solution of this second order differential is

$$\widetilde{U}(u,v,z) = T(u,v)e^{i2\pi\beta z} + R(u,v)e^{-i2\pi\beta z} \tag{3.6}$$

from which the solution of Eq.(3.1) can be found by the inverse Fourier transform

$$U(u,v,z) = \iint_{-\infty}^{\infty} T(u,v)e^{i2\pi(ux+vy+\beta z)}dudv + \iint_{-\infty}^{\infty} R(u,v)e^{i2\pi(ux+vy-\beta z)}dudv. \tag{3.7}$$

The term T describes waves propagating in positive z direction and R describes the backward propagating waves. Propagation factor β of Eq.(3.4) can be either real or an imaginary depending on the magnitude of u^2+v^2. A real propagation factor describes plane waves according to Eq.(3.2) and imaginary propagation factor denotes exponentially increasing or decreasing waves. The representation (3.7) is called Plane Wave Decomposition of an optical field.

If we consider only half space $z \geq 0$, and sources in $z < 0$, we can ignore exponentially increasing and backward propagating waves by writing $R(u,v) = 0$. Now Eq.(3.6) describes an infinite number of plane waves propagating in directions defined by u and v. Now if we consider our reference plane at $z = 0$, then the propagation problem can be formulated as

$$U(u,v,z) = \iint_{-\infty}^{\infty} T(u,v)e^{i2\pi(ux+vy+\beta z)}dudv \tag{3.8}$$

where

$$T(u,v) = \left(\frac{1}{2\pi}\right)^2 \iint_{-\infty}^{\infty} U(x',y',0)e^{-i2\pi(ux'+vy')}dx'dy' \tag{3.9}$$

where x' and y' denote the position coordinates at the plane $z = 0$.

Equation (3.8) is the Angular Spectrum Representation of the field and the quantity $T(u, v)$ in Eq. (3.9) is called the complex angular spectrum of the field at $z = 0$. Since we have not used any approximation, this propagation method is exact in terms of scalar theory. The integrals in Eq. (3.8) and (3.9) can be evaluated numerically using direct and inverse Fast Fourier Transforms (FFT).

The above given equations for angular spectrum representation for scalar fields can also be extended to electromagnetic vector fields. Angular spectrum formulas (3.8)-(3.9) can be applied to electric field components E_x and E_y independently and then E_z can be solved.

3.3 Rayleigh-Sommerfeld propagation

The angular spectrum representation defined by Eqs. (3.8)-(3.9) can be re-written with slightly different notation as

$$U(u, v, z) = \iint_{-\infty}^{\infty} T(p, q) e^{ik(px+qy+mz)} dpdq \tag{3.10}$$

and

$$T(u, v) = \left(\frac{k}{2\pi}\right)^2 \iint_{-\infty}^{\infty} U(x', y', 0)(e^{-ik(px'+qy')} dx'dy', \tag{3.11}$$

where $p = \lambda u, q = \lambda v$ and

$$m^2 = 1 - (p^2 + q^2). \tag{3.12}$$

A combination of Eq.(3.10)-Eq.(3.11) yields

$$U(x, y, z) = \iint_{-\infty}^{\infty} U(x', y') G(x - x', y - y', z) dx'dy', \tag{3.13}$$

where

$$G(x - x', y - y', z)) = \left(\frac{k}{2\pi}\right)^2 \iint_{-\infty}^{\infty} e^{ik[p(x-x')+q(y-y')+mz]} dpdq \tag{3.14}$$

is the Green function of the propagation problem [33]. Denoting $\mathbf{r} = (x, y, z)$ and $\mathbf{r}' = (x', y', 0)$ and using the Weyl representation of spherical wave [33]

$$\frac{e^{ik|\mathbf{r}-\mathbf{r}'|}}{|\mathbf{r} - \mathbf{r}'|} = \left(\frac{ik}{2\pi}\right)^2 \iint_{-\infty}^{\infty} \frac{1}{m} e^{-ik[p(x-x')+q(y-y')+mz]} dpdq \tag{3.15}$$

the Green function Eq. (3.15) can be represented as

$$G(x-x',y-y',z) = -\frac{1}{2\pi}\frac{\partial}{\partial z}\left(\frac{1}{R}e^{ikR}\right), \tag{3.16}$$

where

$$R = \mid r - r' \mid = \sqrt{(x-x')^2 + (y-y')^2 + z^2}. \tag{3.17}$$

Thus the Green function is

$$G(x-x',y-y',z) = -\frac{1}{2\pi}\left(ik - \frac{1}{R}e^{ikR}\right)\frac{z}{R^2}e^{ikR} \tag{3.18}$$

and substitution into Eq. (3.13) gives

$$U(x,y,z) = -\frac{z}{2\pi}\iint_{-\infty}^{\infty} U(x',y',0)\left(ik - \frac{1}{R}e^{ikR}\right)\frac{1}{R^2}e^{ikR}dx'dy', \tag{3.19}$$

which is known as *Rayleigh-Sommerfeld Diffraction Formula*. This propagation method is exact in sense of scalar theory but has a singularity at propagation distance $z = 0$. Thus Rayleigh-Sommerfeld diffraction formula cannot be used for short distances as it will lead to numerical instability.

Rayleigh-Sommerfeld diffraction formula here was derived by angular spectrum representation but it can be derived in many other ways, like starting from Huygen's principle.

3.4 Fresnel diffraction

When the propagating wave travels close to z-axis or has very small divergence, the geometry is said to be *paraxial*. Then MacLaurin expansion of R,

$$R \approx z + \frac{1}{2z}\left[(x-x')^2 + (y-y')^2\right] \tag{3.20}$$

can be used in the exponential term of Rayleigh-Sommerfeld diffraction formula (3.19) and one can write $R \approx z$ in the denominator. The resulting approximate propagation formula is

$$U(x,y,z) = -\frac{ik}{2\pi z}e^{ikz}\iint_{-\infty}^{\infty} U(x',y',0)e^{ik\left[(x-x')^2+(y-y')^2\right]/2z}dx'dy' \tag{3.21}$$

is called *Fresnel diffraction formula*. It can also be derived directly from the angular spectrum representation Eq. (3.10)-(3.11) without using Rayleigh Sommerfeld

diffraction formula. The Fresnel propagation integral is a widely used formula for beam-like wave propagation. With this diffraction formula, several analytical results can be achieved in closed form unlike from the Rayleigh-Sommerfeld diffraction formula. This advantage could be seen in cases like propagation conditions for Gaussian beams where distance between the source and element is greater than Rayleigh length

$$d >> z_r$$

and plane of the element has radius curvature R equal to d in far zone. When the square in the exponential is expanded, the phase factor

$$(x'^2 + y'^2)$$

appears and if it is small it can be ignored. And resulting equation is Fraunhofer propagation formula which is a good approximation in far-field.

3.5 Fast Fourier Transformation algorithm (FFT)

The FFT algorithm can be used for all three above mentioned propagation methods: angular spectrum representation, Rayleigh-Sommerfield diffraction and Fresnel diffraction formula. It reduces the numerical computational time. Equations (3.13) and (3.21) are actually convolutions of two functions

$$(U * G)(x, y) = \iint_{-\infty}^{\infty} U(x', y')G(x - x', y - y', z)dx'dy', \tag{3.22}$$

each of them having different Green Function G. Thus, from the property of convolutions,

$$\mathcal{F}\{U * G\} = \mathcal{F}\{U\}\,\mathcal{F}\{G\}\,. \tag{3.23}$$

The Fourier transform of the final field $U(x, y, z)$ is the product of the Fourier transforms of the initial field $U(x', y', 0)$ and the Green function $G(x - x', y - y', z)$ associated with the propagation problem. Due to inherent periodicity of FFT algorithm, it is very useful for analyzing periodic fields. For non-periodic fields zero padding should be done in element plane.

3.6 Complex amplitude transmittance approach (CATA)

This approach treats the diffractive element as a thin screen that modulates the amplitude, phase, and sometimes also the polarization properties of the incident field. We can use this method, when the thickness of the grating profile is of the order of wavelength and minimum feature size is larger than 10λ, otherwise rigorous grating analysis methods such as the Fourier Modal Method (FMM) [34, 35] should be used. CATA can also be used for the analysis of non-periodic structures.

Complex amplitude transmittance approach states that the scalar incident field $U_i(x, 0)$ and the transmitted field $U_t(x, t)$ are related to each other as

$$U_t(x, t) = t(x)U_i(x, 0), \tag{3.24}$$

where $t(x)$ is the complex amplitude transmission function and t is the thickness of the element. The complex refractive index is defined as

$$\hat{n}(x, z) = n(x, z) + i\kappa(x, z), \tag{3.25}$$

where $n(x, z)$ is the real refractive index and $\kappa(x, z)$ is the absorbtion coefficient. If the thickness t is small, it can be said that the propagating wave is affected only by point wise amplitude and phase change. If the area is fully transparent or non conductive, i.e., $\kappa = 0$, the element only affects the phase of the incident field (phase only element). The function $t(x)$ can then be determined by calculating optical path at each point of the element:

$$t(x) = \exp\left[ik \int_0^t \hat{n}(x, z)dz\right]. \tag{3.26}$$

In this thesis only phase only diffractive elementss are considered. For a periodic structure the complex amplitude transmission function can be expressed in Fourier expansion as

$$t(x) = \sum_{m=-\infty}^{\infty} T_m \exp\left(\frac{i2\pi mx}{d}\right), \tag{3.27}$$

where the Fourier coefficients T_m are obtained from

$$T(m) = \frac{1}{d}\int_0^d t(x) \exp\left(\frac{-i2\pi mx}{d}\right) dx, \tag{3.28}$$

where d is the grating period and m is the diffraction order. Diffraction efficiency of mth diffraction orders is given by

$$\eta_m = |T_m|^2 \tag{3.29}$$

if we ignore Fresnel reflection losses.

3.7 Gaussian beams

This thesis deals with input Gaussian beam, so before starting with the design part a brief overview on Gaussian beams and their parameter [32] is given here. A field propagating as a modulated plane wave in z direction can be expressed as,

$$U(\mathbf{r}) = A(\mathbf{r}) \exp(ikz), \tag{3.30}$$

where $A(\mathbf{r})$ modulating plane wave, k is propagation constant along z direction. Helmholtz equation and slowly varying approximation gives,

$$\frac{d^2A(\mathbf{r})}{d^2x} + \frac{d^2A(\mathbf{r})}{d^2y} - 2ik\frac{d}{dz}A(\mathbf{r}) = 0. \tag{3.31}$$

Gaussian beams are the one of solution of the paraxial wave equation,

$$A(\mathbf{r}) = \frac{A_1}{q(z)} \exp\left(ik\frac{\rho^2}{2q(z)}\right), \tag{3.32}$$

where $\rho^2 = x^2 + y^2$, A_1 is constant and the parameter $q(z)$ can be expressed in the form

$$\frac{1}{q(z)} = \frac{1}{R(z)} - i\frac{\lambda}{\pi w(z)^2}. \tag{3.33}$$

Here $R(z)$ is radius of curvature of phase and $w(z)$ is the width of the Gaussian function. On inserting the Eq. (3.32) into Eq. (3.30) gives full wave equation,

$$U(\mathbf{r}) = A_0\frac{w}{w(z)} \exp\left(\frac{\rho^2}{w(z)^2}\right) \exp\left(ikz - ik\frac{\rho^2}{2R(z)} - i\varsigma(z)\right), \tag{3.34}$$

where

$$w(z) = w_0\sqrt{1 + (z/z_R)^2}, \tag{3.35}$$

$$R(z) = z\left(1 + (z/z_R)^2\right), \tag{3.36}$$

$$\varsigma(z) = \tan^{-1} \frac{z}{z_R}, \tag{3.37}$$

$$w_0 = \sqrt{\frac{\lambda z_R}{\pi}}, \tag{3.38}$$

and

$$A_0 = \frac{A_1}{i z_R}. \tag{3.39}$$

w_0 is beam width which is defines as the width of beam at $z = 0$, z_R is Rayleigh range and $\varsigma(z)$ is phase delay.

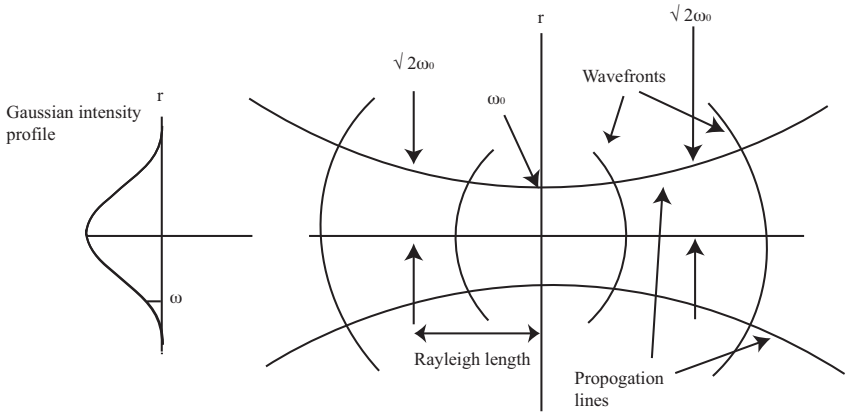

Figure 3.1: A Gaussian beam radial intensity profile and its spherical wavefronts.

Chapter IV

Optical map transform

The principle of optical map transform was first given by Kurtz *et al.* [12] and was further discussed in [1,7,10]. A schematic of one dimensional map transform is given in Fig. 4.1. Element phase $\Phi(x)$ is found from map transform such that when applied to incident intensity distribution $I_1(x', 0)$, it gives the desired intensity distributions $I_2(x, z)$. From energy conservation law, total energy in incident and desired intensity distribution should be same i.e.,

$$\int_{-\infty}^{\infty} I_1(x)dx = \int_{-\infty}^{\infty} I_2(u)dx. \tag{4.1}$$

Both the intensity distributions are divided into N pieces such that each piece contains the same amount of energy. Optical mapping is done $x \longrightarrow x$ such that it finds the phase $\Phi(x)$ which deflects light incident on point x_n to point u_n, where $n = 1, 2, 3, ...N$. The direction of propagation of plane wave or ray connecting x_n and u_n can be considered as the direction of the diffraction order $m = -1$ of local grating given by

$$\sin \Theta_{-1}(u) = -\frac{\lambda}{d(u)}\frac{u}{z}, \tag{4.2}$$

where $d(u)$ is local period, defined by

$$\frac{1}{d(u)} = \frac{1}{2\pi}\frac{d\Phi(u)}{du} \tag{4.3}$$

when $N \to \infty$. Thus in paraxial geometry, we get

$$d\Phi(x) = \frac{2\pi}{\lambda z}(u - x)dx \tag{4.4}$$

The mapping $x \longrightarrow u$ can be found by integration

$$\int_{x_0}^{x} I_1(\xi')d\xi' = \int_{u_0}^{u} I_2(\xi)d\xi \tag{4.5}$$

The optical map transform is a good approach for paraxial design but if the geometry

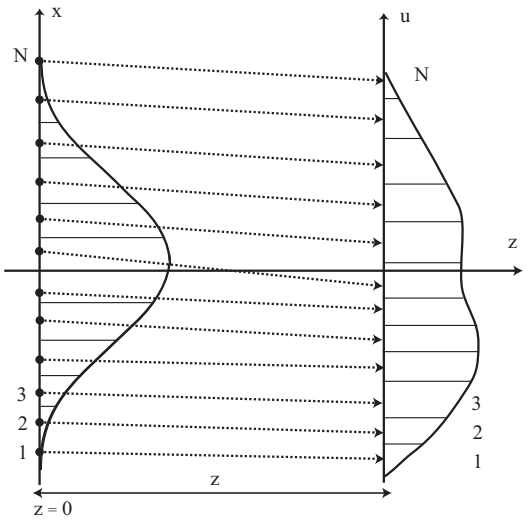

Figure 4.1: Principle of optical map transform

is not paraxial then one has to do it numerically, and elements designed by it are sensitive to fabrication and alignment errors.

Throughout this thesis we have talked about transforming the Gaussian beam into exact flat-top and super-Gaussian. This is because field emitted by lasers typically have Gaussian profile and we often want to transform them to uniform intensity profile. Before starting with the design part, let us give an overview what exact flat-top and super-Gaussian means. When we are talking about exact flat-top we mean intensity or field distribution with sharp edges but super-Gaussian has rounded edges and it becomes sharper with the increase in order N.

$$I(x) = \exp\left(\frac{-x}{w}\right)^{\mathrm{N}} \tag{4.6}$$

And $N = 2$ is a Gaussian and when $N \to \infty$ it becomes exact flat-top. Fig. 4.2 shows the super-Gaussian profile with different order N.

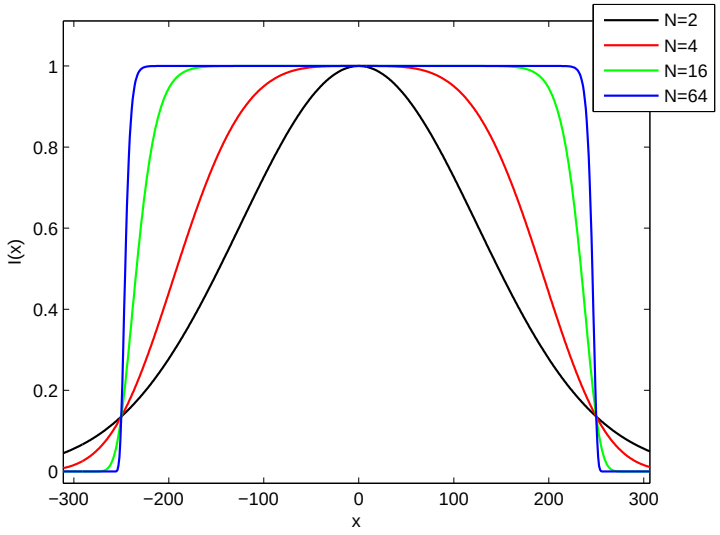

Figure 4.2: Super-Gaussian function with different order N.

4.1 Design examples

4.1.1 Paraxial beam shaping case

The task is to convert a plane wave with Gaussian intensity distribution to a flat top or super-Gaussian intensity profile for rotationally symmetric and y-invariant geometries. The distance of propagation is of the order of 100 mm. In this thesis geometrical beam shaping is done analytically and numerically. The design of one dimensional beam shaping element is discussed first, where the light along one axis of an incoming Gaussian beam is turned into flat top profile and the design parameters are given in table 4.1.

Gaussian to flat-top

The incident field $U_i(x, y, z_i)$ and the signal field $U_s(x, y, z_s)$ are normalized such that their energies are equal to unity. For rotationally symmetric geometry the field are normalized as

$$2\pi \int_0^\infty \mid U_i(r, z_i) \mid^2 r dr = 1 \tag{4.7}$$

Table 4.1: Table of specification

Parameter	Value
Wavelength(nm)	633
Input beam shape	Axial Symmetrical Guassian beam
Input beam waist	555 μm
Output beam shape	Flat top
Propagation distance	30-100 mm

and

$$2\pi \int_0^{\infty} \mid U_s(\rho, z_s) \mid^2 \rho d\rho = 1, \tag{4.8}$$

where $r = \sqrt{(x^2 + y^2)}$ and $\rho = \sqrt{(u^2 + v^2)}$. The energy balance condition is

$$\int_0^{r} \mid U_i(r', z_i) \mid^2 r' dr' = \int_0^{\rho} \mid U_s(\rho', z_s) \mid^2 \rho' d\rho' \tag{4.9}$$

The normalization of the Gaussian incident field

$$2\pi \int_{-\infty}^{\infty} U_i(r') exp\left(\frac{-2r^2}{w^2}\right) r dr = 1, \tag{4.10}$$

leads to

$$U_i = -\frac{\omega^2 \pi}{2}. \tag{4.11}$$

The flat-top field is

$$U_s(\rho', z_s) = \begin{cases} U_s & \text{if } |\rho| \leq a^2 \\ 0 & \text{otherwise} \end{cases} \tag{4.12}$$

and its normalization gives

$$|U_s|^2 = \frac{\pi}{a^4}. \tag{4.13}$$

In accordance with the map-transform principle, we divide the incident intensity $I_i(x)$ and the signal intensity $I_s(u)$ into N parts each containing equal amount of energy. The DE then redirects the incident ray in such a way that light from each part in the x-plane is directed towards corresponding part in u-plane. Now, we consider y-invariant element geometry and energy balance condition or mapping condition $x \rightarrow u(x)$ given in Eq. (4.14) and in Fig. 4.3:

$$\int_0^{x} \mid U_i(x', z_i) \mid^2 dx' = \int_0^{u(x)} \mid U_s(u', z_s) \mid^2 du' \tag{4.14}$$

or

$$\int_0^x I_i(x', z_i)dx' = \int_0^{u(x)} I_s(u', z_s)du' \tag{4.15}$$

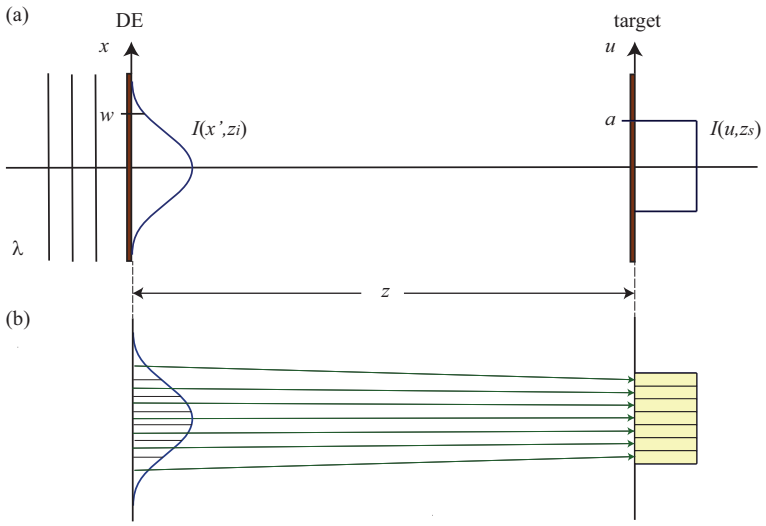

Figure 4.3: Principle of optical map-transform. (a) Optical function: Gaussian to flat-top transformation. (b) Model for numerical construction of the phase function.

The DE converts the normally incident ray at each point x into a ray that propagates at an angle θ given by

$$\tan\theta = \frac{u(x) - x}{\triangle z}. \tag{4.16}$$

The input field has constant phase and $\Phi(x)$ is the phase function of DE. The local

ray direction is normal to the constant phase of the field just after the DE. We have

$$\sin\theta = \frac{1}{k}\frac{d\Phi(x)}{dx} \tag{4.17}$$

and by integrating

$$\Phi(x) = \frac{k}{\triangle z}\int_0^x [u(x') - x]dx'. \tag{4.18}$$

Equation (4.18) is the phase function of the element for the first non-paraxial geometry. Phase function of the element generated by map transform is shown in Fig. 4.4(a). Here the minimum feature size is more than 5 microns, which is realizable for fabrication. After propagation the flat-top profile generated is shown in Fig. 4.4(b)and for smoother flat top super-Gaussian profile phase is shown in Fig. 4.4(c) and flat-top is shown in Fig. 4.4(d).

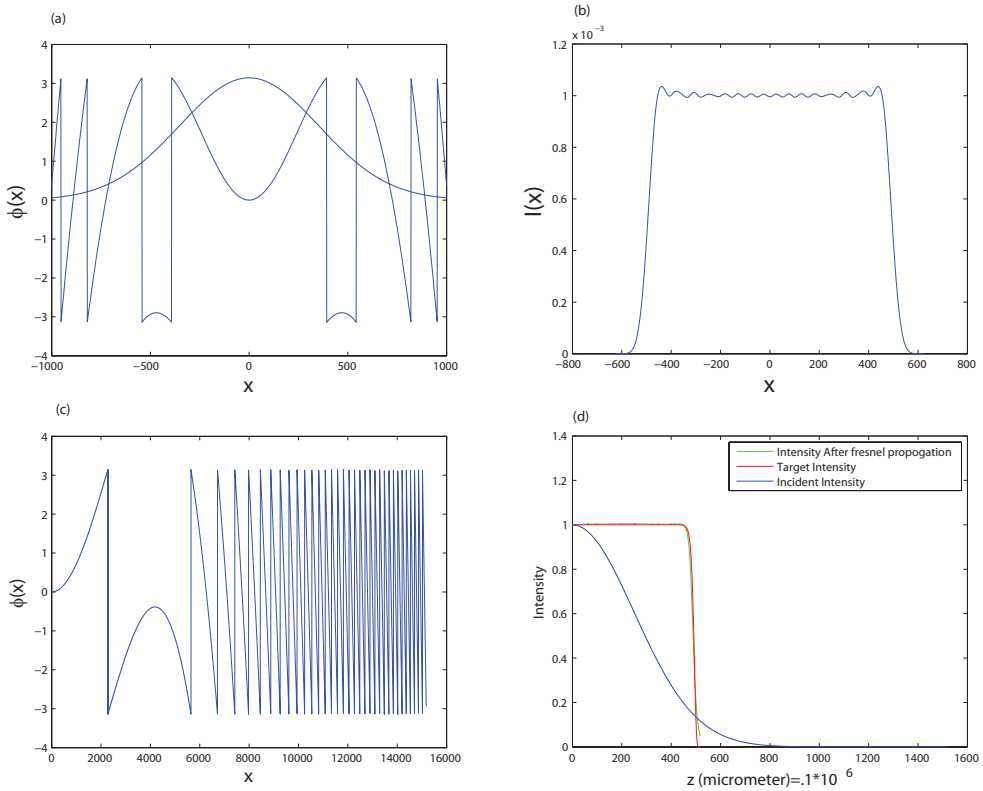

Figure 4.4: Gaussian to flat-top transformation (a) Phase function of one dimensional diffractive element generated by map-transform and incident field intensity profile for exact flat-top transformation. (b) The intensity profile at the target plane obtained by Fresnel propagation integral. (c) Phase function of one dimensional diffractive element generated by map-transform and incident field intensity profile for Super-Gaussian transformation for $N = 64$. (d) The intensity profile at the target plane obtained by Fresnel propagation integral numerically by transforming Gaussian to Super-Gaussian. The horizontal axis x is taken in μm.

The phase function of Eq. (4.18) is in general calculated numerically and target field can be exact flat top, super-Gaussian or anything. The analytical $\Phi(x)$ is easy to obtain for exact flat-top. For super-Gaussian a numerical procedure needs to be used [20]. Numerical phase function calculation is easier for super-Gaussian profile of any power N. Fig. 4.4(a) is the analytical phase of DE for exact flat top profile.

Here target distribution is $I(u) = \frac{1}{2a}$, $0 < u < a$, where a is chosen to be 500 μm and z is propagation distance. The analytical phase for Gaussian to exact flat-top conversion is

$$\phi(x) = \frac{2\pi}{\lambda z}\left(a\omega\frac{-1+exp(-2x^2/\omega^2)}{\sqrt{2\pi}} - \frac{x^2}{2} + axerf\frac{\sqrt{2}x}{\omega}\right). \tag{4.19}$$

Now, with the same parameters of 1D solution, it can be crossed to get rectangular flat-top profiles. For two dimensional rectangular case phase function is

$$\Phi(x,y) = \Phi(x)\Phi(y) \tag{4.20}$$

where both $\Phi(x)$ and$\Phi(y)$ are of the form of Eq.(4.19). Three propagation method namely angular spectrum representation, Rayleigh Sommerfeld diffraction and Fresnel diffraction were used to evaluate the quality of the flat top profile in target plane. The results presented in Fig. 4.5(a)-Fig. 4.5(c) all three methods give essentially similar results.

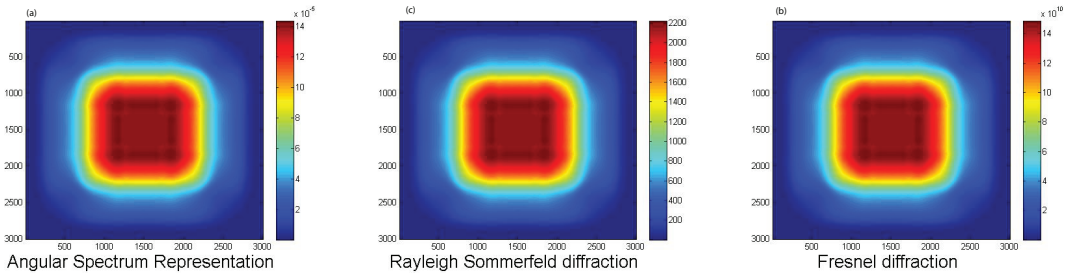

Figure 4.5: Diffraction patterns produced by the map-transform element in Fig. **??** evaluated by three different methods: (a) Angular spectrum representation, (b) Rayleigh–Sommerfeld diffraction formula, and (c) Fresnel diffraction formula.

Fig.4.5 shows the exact flat-top profile as the target, but also illustrates intensity variations within the target profile revealed by the wave-optical analysis. In order to get smoother flat top incident Gaussian beam was transformed to super Gaussian profile in target as seen in Fig.4.6. Here in Fig. 4.6(a), the super-Gaussian order N is chosen to be 16 and in Fig. 4.6(b) it is chosen to be 32.

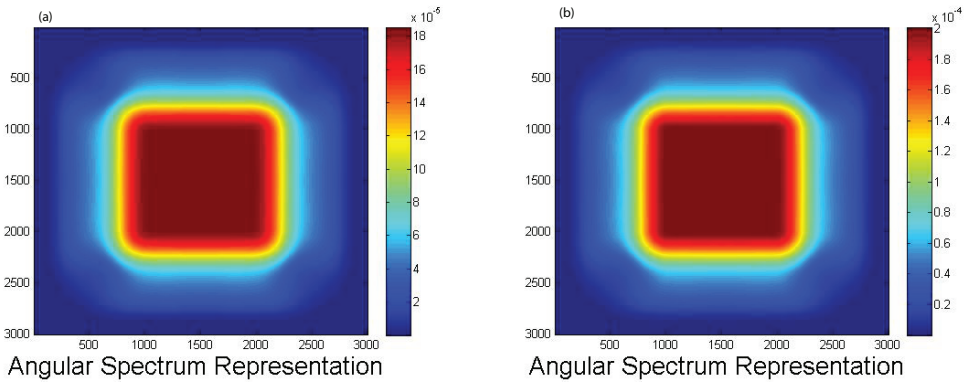

Figure 4.6: Diffraction patterns produced by the map-transform element evaluated for super Gaussian target profile (a) of order N=16, (b) and of order N=32.

4.1.2 Far-field beam shaping case

In far-field, if we are dealing with non-paraxial case, we assume that the laser emits a non-paraxial Gaussian beam and we can treat this laser or its image as a point source. We assume that the cylindrical lens is used to collimate the field in y-direction. Map transform between input angle θ and output divergence angle θ' in far field should convert incident intensity profile into flat top profile in the far field, i.e, in k_x space as illustrated in Fig. 4.8. And input parameter are given in table. 4.2.

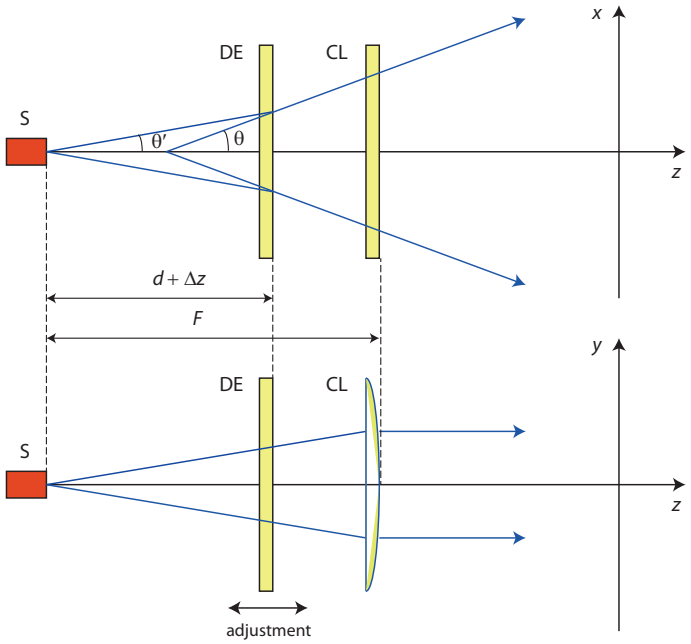

Figure 4.7: Light incident from point source to the DE and Δz is a longitudinal position error, where d is distance between the source and DE. CL is cylindrical lens which collimates the beam in y and gives flat-top profile in x direction.

Here incident ray at angle θ' is transformed to into a ray at angle θ, for our far field $k_x = k \sin\theta$ and maximum divergence angle Φ with $k_x = k \sin\Phi$.

Table 4.2: Table of specification

Parameter	Value
Wavelength(nm)	633
Distance between source and element(d)	3000 μm
Input divergence angle	10^0
Output divergence angle	10^0
Propagation distance	Far field

Gaussian to exact Flat top transformation

Gaussian to exact Flat top: Target intensity distribution is given below, where Φ is the divergence angle:

$$I_{\mathrm{s}}(k_x) = \begin{cases} I_{\mathrm{s}} & \text{if } |k_x| \leq |k \sin \Phi| \\ 0 & \text{otherwise} \end{cases} \tag{4.21}$$

So that we have a flat-top profile over an angular range $-\Phi \leq \theta \leq +\Phi$ where Φ is chosen to be 10^o.

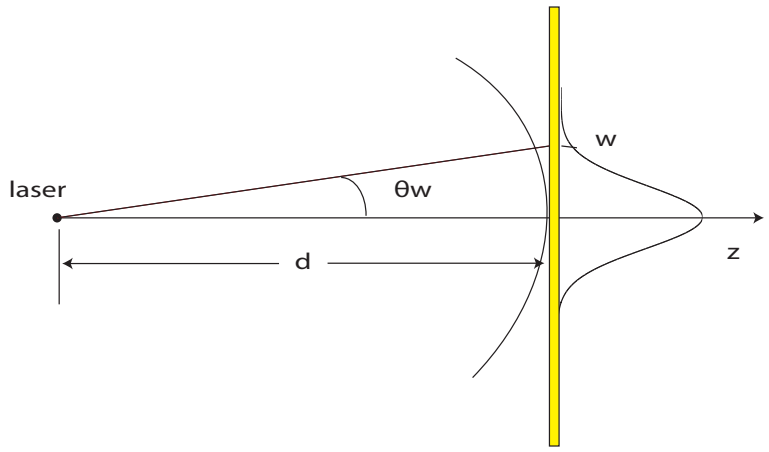

Figure 4.8: Light incident from point source to the DE, where d is distance between the source and DE which is larger than the emitting area of the source.

where d is distance between the source and DE which is larger than the emitting area of the source. $w = d \tan \theta_w$ and $\theta_w = 10^o$.

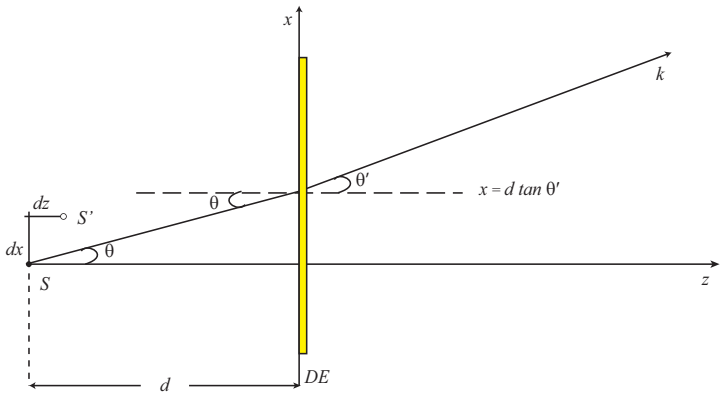

Figure 4.9: Gaussian to flat-top transformation in far zone or k_x space. Here S is point source and S' is displaced source position and dx is lateral displacement and dz is longitudinal displacement of the source.

Incident field is a diverging spherical wave with radius of curvature $R = d$. Incident intensity profile is given below and in principle we have a non-paraxial Gaussian input beam :

$$I_i(x) = I_i \exp\left(\frac{-2x^2}{\omega^2}\right). \tag{4.22}$$

We deal with one dimensional symmetry as we consider that it is collimated in y axis. We normalize our incident field $I_i(x)$ and the signal field $I_s(k_x)$ as follows .

$$\int_{-\infty}^{\infty} I_i(x)dx = 1. \tag{4.23}$$

Thus,we get

$$I_i = \sqrt{\frac{2}{\pi}}\frac{1}{\omega}. \tag{4.24}$$

Normalizing the target field by

$$\int_{-\infty}^{\infty} I_s(k_x)dk_x = 1 \tag{4.25}$$

we get

$$I_s = \frac{1}{2k\Phi}. \tag{4.26}$$

.

From map-transform relation we get following relation, i.e., the energy balance condition is given by

$$\int_0^x I_i(x')dx' = \int_0^{k\theta'} I_s(k_{x'})dk_{x'}. \tag{4.27}$$

Integrating this we get

$$\operatorname{erf}\left(\frac{\sqrt{2}x}{\omega^2}\right) = \frac{\theta'}{\Phi}. \tag{4.28}$$

Phase function of the element can be found using non paraxial form of grating equation. We have,

$$\sin\theta' = \sin\theta + \frac{1}{k}\frac{d}{dx}\Phi(x) \tag{4.29}$$

and using paraxial form

$$\theta' = \theta + \frac{1}{k}\frac{d}{dx}\Phi(x), \tag{4.30}$$

where $\Phi(x)$ is element phase function, such that $\theta \approx \tan\theta = \frac{x}{d}$ and $\theta' \approx \sin\theta' = \frac{k_x}{k}$. And we consider unit refractive index on both side of the DE.

$$k_x = \frac{k}{d}x + \frac{d}{dx}\Phi(x), \tag{4.31}$$

which gives

$$\Phi(x) = \int_0^x \left(k_x - \frac{k}{d}x'\right)dx' \tag{4.32}$$

and thus can be solved analytically. We get

$$\Phi(x) = k\left\{\frac{\Phi w}{\sqrt{2\pi}}\left[\exp\left(\frac{-2x^2}{w^2}\right) - 1\right] - \frac{x^2}{2d} + \Phi x \operatorname{erf}\left(\frac{\sqrt{2}x}{w}\right)\right\}. \tag{4.33}$$

Numerical simulation of map-transform is given below

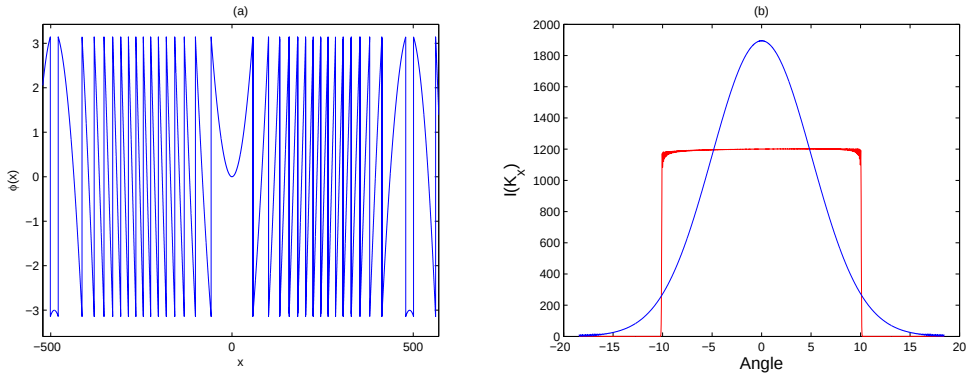

Figure 4.10: (a) Phase function of one dimensional diffractive element generated from map-transform. (b) Intensity distribution of exact flat top profile with $\Phi(x)$ generated analytically, here blue curve shows the far-field profile without an element.

Gaussian to super Gaussian

Map transform has been done numerically here. Parameters are same as used in table. 4.2. Incident field is also same as in Eq. (4.22), and the target field is a super-Gaussian with power $N = 64$:.

$$I_s(x) = I_s \exp\left(\frac{-2x^2}{w_o^2}\right)^{64}. \tag{4.34}$$

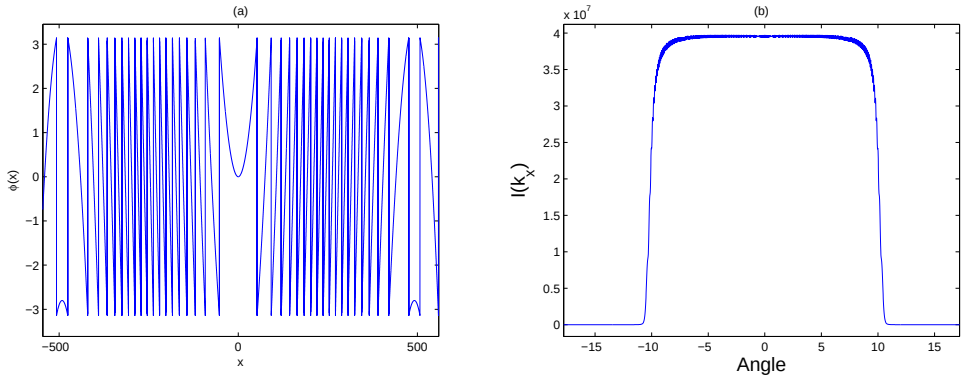

Figure 4.11: (a) Phase function of one dimensional diffractive element generated from map-transform numerically, which is almost identical to analytical phase profile shown in Fig.4.10(a). (b) Intensity distribution of super-Gaussian profile generated numerically, with $N = 64$.

Now the phase function is more complicated than in the Fresnel case, hence feature size is smaller. Small ripples appear in the flat-top region.

Chapter V

Tolerance analysis

Tolerance analysis is very important as the map transform elements are very sensitive to lateral and longitudinal misalignment. As these elements are designed to redistribute intensity a small fraction of deviation in source intensity distribution from designed shape has noticeable effect on obtained target intensity distribution. The fabricated flat-top elements suffer from sensitivity to fabrication errors such as profile shape and height errors. The effect of these error is so big that it introduces the zeroth diffraction order and hence produces an unwanted central intensity peak and intensity ripple.

5.1 Near-Field: Lateral and longitudinal displacement

We assume that the source is displaced laterally by Δx and longitudinally by Δz from its original position and our incident field has planar phase front. Then the incident field has the expression

$$U(x) = \exp\left[-\frac{(x-\Delta x)^2}{w_o^2(1-\frac{\Delta z}{d})^2}\right]. \tag{5.1}$$

.

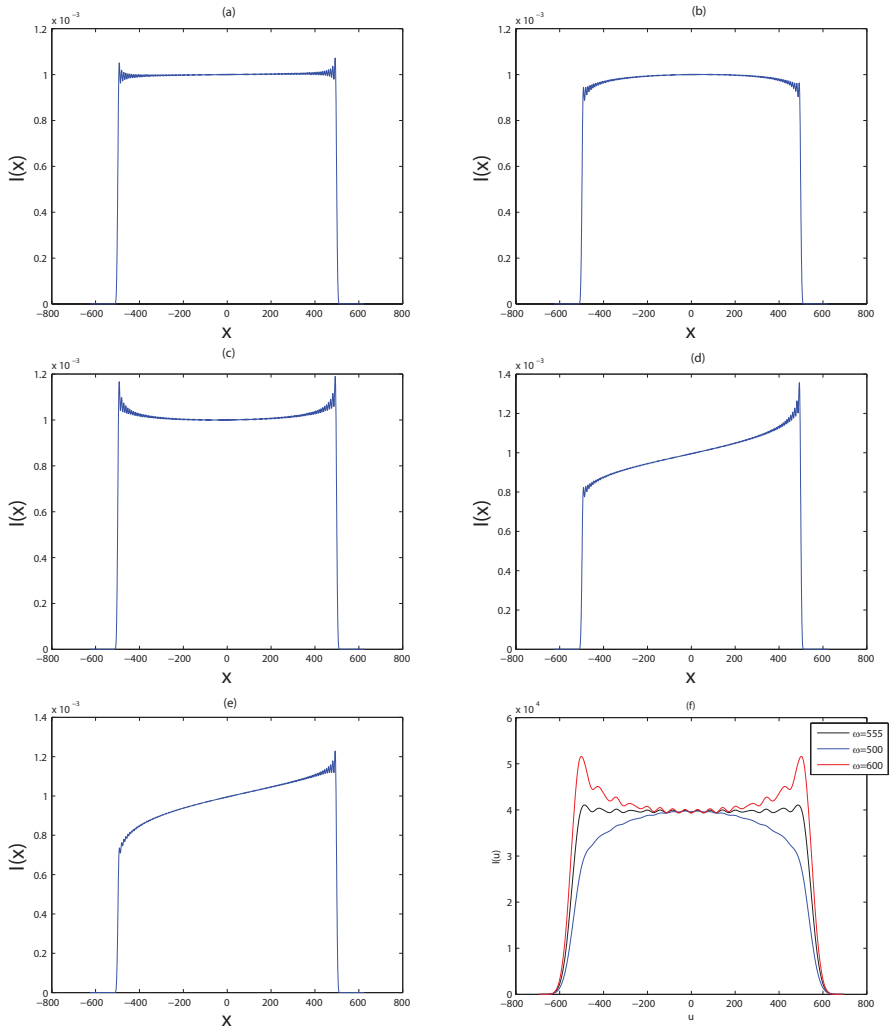

Figure 5.1: Near-field beam shaping for exact Flat top (a) Target diffraction pattern when the element is in correct longitudinal and lateral position. Intensity profile when the source is (b) too close to the element by an amount $\Delta z = 100\ \mu m$, (c) too far from the element by an amount $\Delta z = 100\ \mu m$, (d) at correct longitudinal position but laterally displaced by an amount$\Delta x = 25\ \mu m$, (e) The lateral displacement is $\Delta z = 100\ \mu m$ and longitudinal displacement is $\Delta x = 25\ \mu m$, (f) for different beam waist, correct beam waist w is 555 μm.

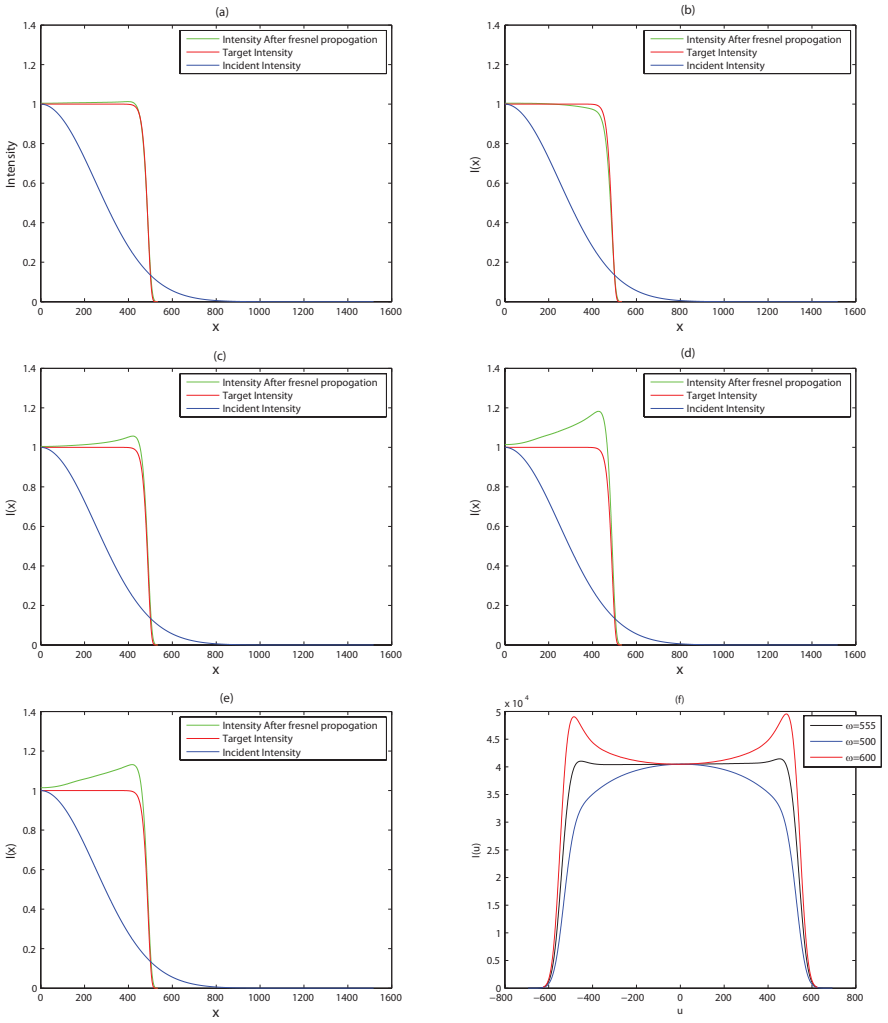

Figure 5.2: Near-field beam shaping done numerically for super-Gaussian (a) Target diffraction pattern when the element is in correct longitudinal and lateral position. Intensity profile when the source is (b) too close to the element by an amount $\Delta z = 100\ \mu m$, (c) too far from the element by an amount $\Delta z = 100\ \mu m$, (d) at correct longitudinal position but laterally displaced by an amount$\Delta x = 25\ \mu m$, (e) The lateral displacement is $\Delta z = 100\ \mu m$ and longitudinal displacement is $\Delta x = 25\ \mu m$, (f) for different beam waist, correct beam waist w is 555 μm.

From the figures we can see that the small misalignment makes the intensity

profile asymmetric. It was seen that positive values $\Delta z > 0$ (distance between S and DE too large) and an increase in w above its design value both lead to edge enhancement in the shaped profile. Correspondingly, negative values of Δz and a decrease in w gave rise to rounding of the desired flat-top profile. Therefore we can compensate for variations in w simply by adjusting Δz slightly in the assembly phase of the setup in order to get a nice flat-top profile in the Fresnel domain. The acceptable variation in w is $+/-10$ μm from the actual w.

5.2 Far-field: Lateral and longitudinal displacement

We assume that the source is displaced laterally by Δx and longitudinally by Δz from its original position. The transmitted field depends upon incident field and complex amplitude transmittance of the element, which is fixed. So only the incident field contains the lateral and longitudinal displacement factor, which can be written as

$$U(x) = \exp\left[-\frac{(x-\Delta x)^2}{\omega_o^2(1-\frac{\Delta z}{d})^2}\right]\exp\left[i\frac{k_0(x-\Delta x)^2}{2(d-\Delta z)}\right]. \tag{5.2}$$

.

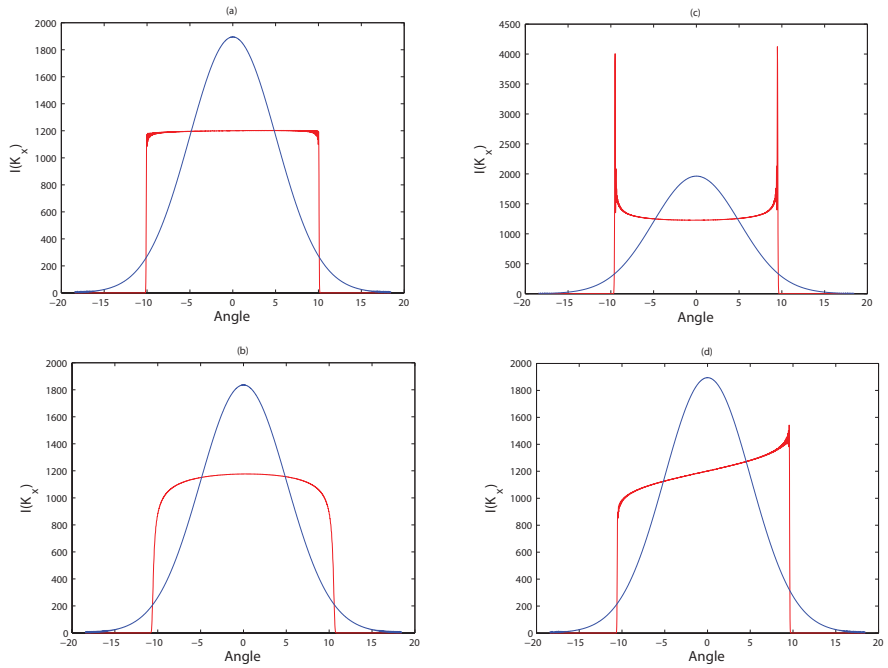

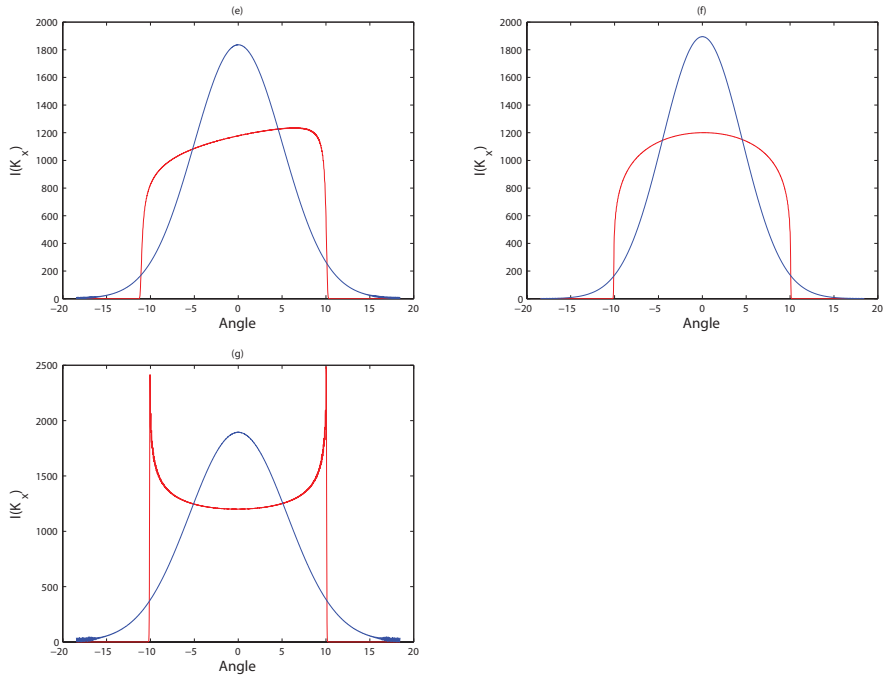

Figure 5.3: Far field beam shaping (a) Target diffraction pattern when the element is in correct longitudinal and lateral position. Intensity profile when the source is (b) too close to the element by an amount $\Delta z = 100\ \mu m$, (c) too far from the element by an amount $\Delta z = 100\ \mu m$, (d) at correct longitudinal position but laterally displaced by an amount$\Delta x = 25\ \mu m$, (e) The lateral displacement is $\Delta z = 100\ \mu m$ and longitudinal displacement is $\Delta x = 25\ \mu m$. In(a)-(e) the blue curves show the far field profile without element and red curve show far field profile with element. (f) Input Divergence angle change by $-1°$ i.e $9°$.(g) Input Divergence angle change by $+1°$ i.e $11°$.

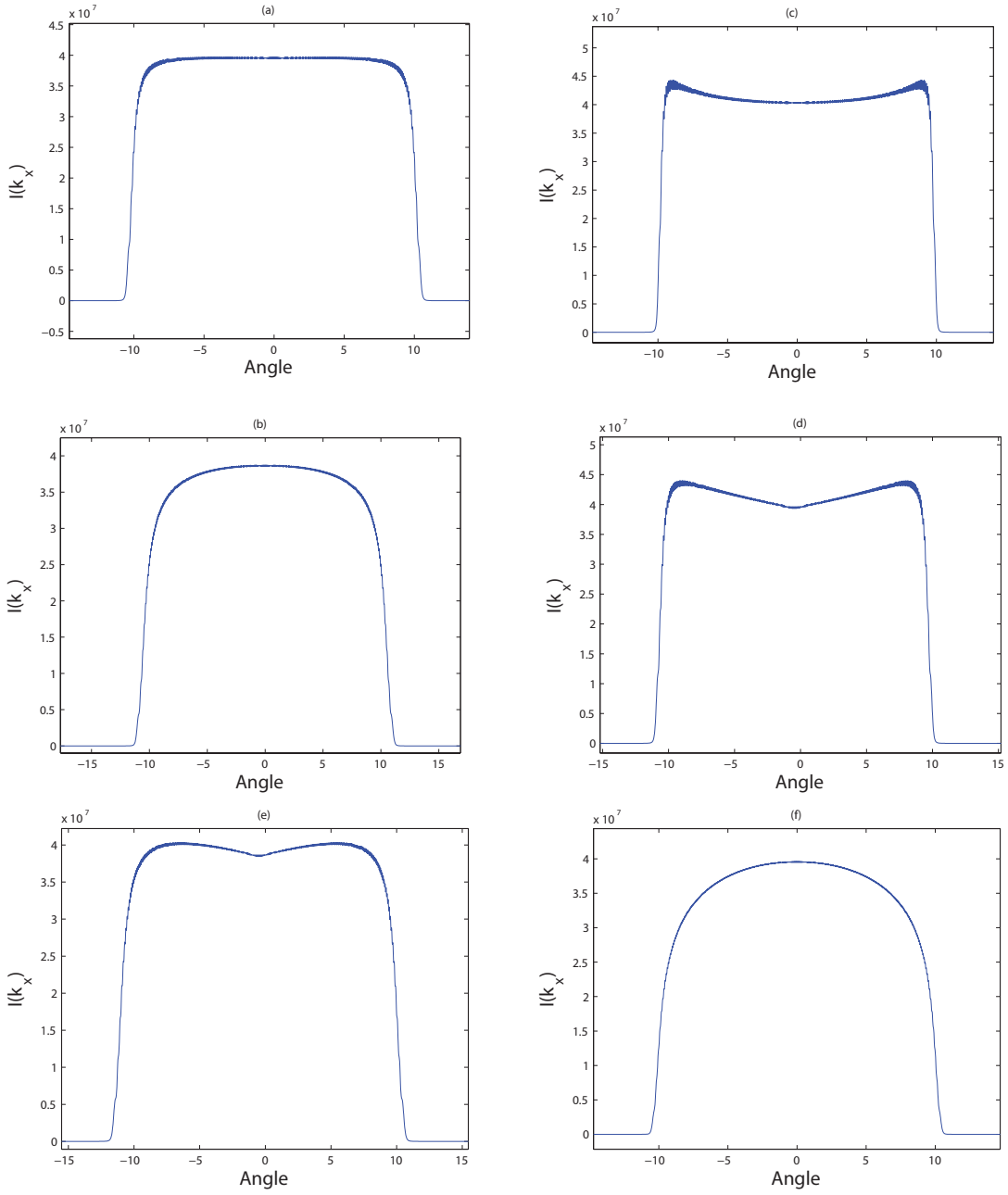
(a)
x 10^7
I(k_x)
Angle
(c)
x 10^7
I(k_x)
Angle
(b)
x 10^7
I(k_x)
Angle
(d)
x 10^7
I(k_x)
Angle
(e)
x 10^7
I(k_x)
Angle
(f)
x 10^7
I(k_x)
Angle

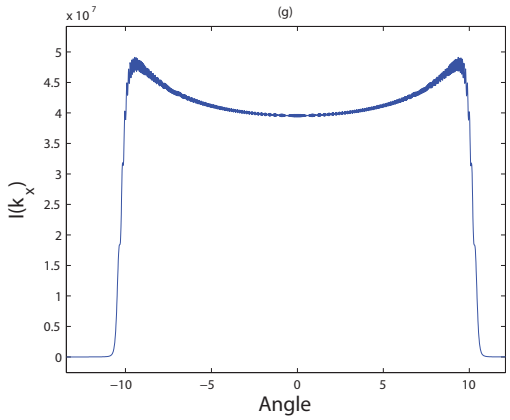

Figure 5.4: Far field beam shaping done numerically giving Super-Gaussian in far field (a) Target diffraction pattern when the element is in correct longitudinal and lateral position. Intensity profile when the source is (b) too close to the element by an amount $\Delta z = 100\mu m$, (c) too far from the element by an amount $\Delta z = 100\mu m$, (d) at correct longitudinal position but laterally displaced by an amount$\Delta x = 25\mu m$, (e) The lateral displacement is $\Delta z = 100\mu m$ and longitudinal displacement is $\Delta x = 25\mu m$. (f) Input divergence angle change by -1° i.e 9°. (g) Input Divergence angle change by $+1^\circ$ i.e 11°.

From the figures we can see that the small misalignment makes the intensity profile asymmetric. It was seen an increase in θ above its design value both lead to edge enhancement in the shaped profile. Correspondingly, a decrease in θ gave rise to rounding of the desired flat-top profile. Therefore we can compensate for variations in θ simply by adjusting Δz slightly in the assembly phase of the setup in order to get a nice flat-top profile in the far field without a significant effect in the final fan angle Φ.

Chapter VI

Characterization and fabrication errors

The key to a successful design is correct simulation, realization of simulated function by fabrication, characterization of the element to check if the element gives the desired output and the final step is the possibility of redesign if the desired output is not obtained. All the steps are discussed in detail in this chapter.

6.1 Simulation

All the designs were simulated in MATLAB and was discussed in chapter IV and there tolerances in chapter V. In order to verify that the codes were generated properly, analytical map transform phase functions were simulated numerically and analytically. And they were matched. For example in Fig. 6.1 Gaussian to Gaussian transformation is done using map transform method analytically and numerically.

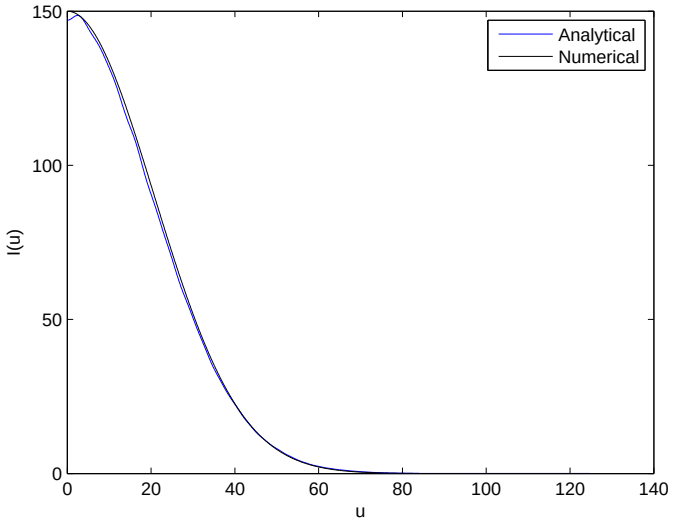

Figure 6.1: Gaussian to Gaussian transformation using map transform method. Field was propagated using Fresnel diffraction formula.

It can be seen from the Fig. 6.1 that analytical transformation and numerical transformation give the same result. Thus, simulated design can be considered correct.

6.2 Fabrication

Based on the design and simulation results for the flat-top, diffractive phase elements for this work was fabricated by Janne Laukkanen using electron beam lithography. Electron beam lithography also known as e-beam lithography is direct write technique used for nanometer scale resolution [36]. The fabrication procedure is explained in Fig. 6.2.

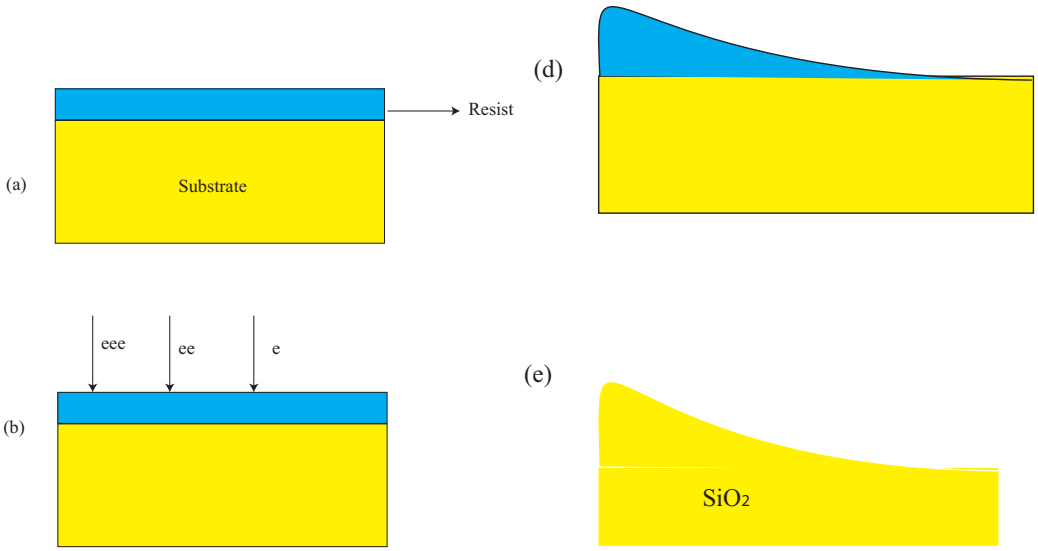

Figure 6.2: Fabrication steps of analog grating profile with proportional reactive ion etching. (a) Substrate preparation with resist coating. (b) Exposure. (c) Development. (d) Reactive ion etching.

First substrate is spin coated with resist layer. After spinning of resist layer, it is exposed with negative resist (gray scale-ARN 7720). Different dose is applied, during development stage that part which have maximum dose dissolves less compared to less exposed part. Reactive ion etching(RIE) is used to etch the profile so long that the resist is gone and we are left with analog profile. RIE is a good technique for high precision anisotropic etching, but however a small isotropy remains which can lead to loss of dimensions.

The fabrication procedure can produce different kinds of errors like substrate figure error, pattern distortion error, duty-cycle error, etching depth error and surface roughness error [37]. Surface roughness error is of no concern here as we consider that amplitude is unity and we have only phase. In this work etching depth error is of concern as design height t was not similar to fabricated height t'. Fig. 6.3 shows the triangular grating with parameters period dp, design height t and etch height t'.

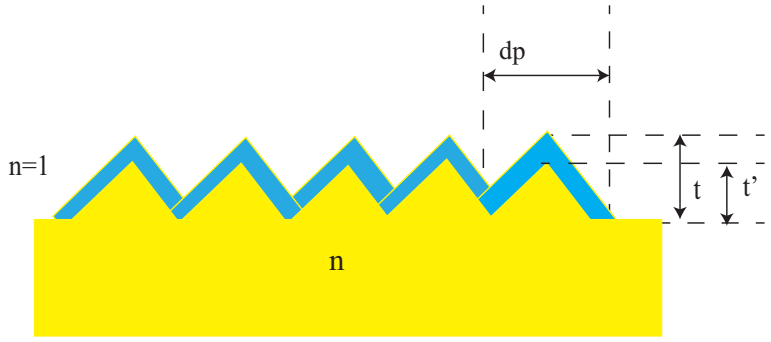

Figure 6.3: Triangular grating profile.

Figure 6.4 shows a small portion of the simulated and measured phase profile. From the figure we can see that simulated profile has sharp edges and the profile height is 1.3 μm. However, the fabricated profile have rounded edges, non-uniform etch height and profile curved in wrong direction. From the analysis of fabricated phase profile, it was found that the average etch height in the central area is 0.808 μm and in the corners it was 0.7 μm showing standard deviation of 0.07. Images of the phase profile were taken using 3-D optical profiler. Far-field phase profiles were comparatively better than Fresnel-domain elements phase profile. Reason behind the difference in far-field and Fresnel-domain element phase profile was the improper sampling points and maybe the fabrication process was not well calibrated in these experiments. Fig. 6.5 shows the improper sampling points in Fresnel domain and far-field phase, it can be seen that sampling point error affect the near-field phase more compared to far field element.

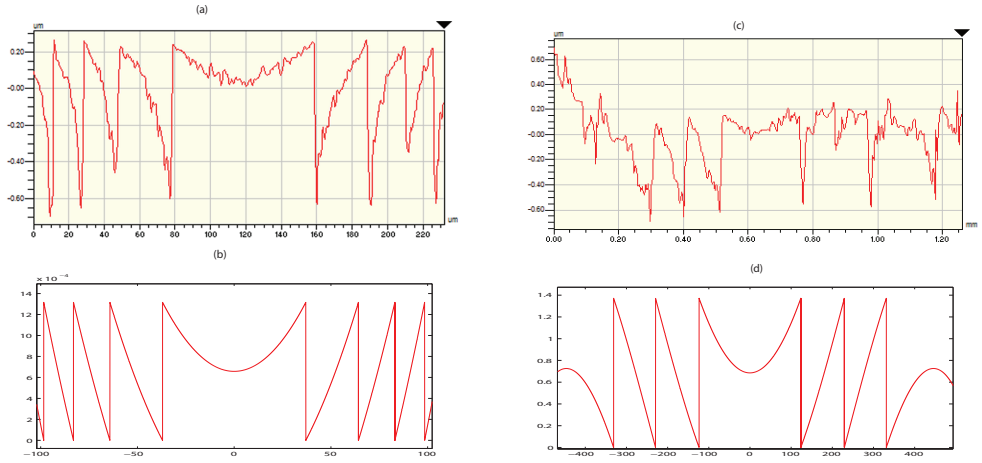

Figure 6.4: Phase profile:(a) measured. (b) simulated. (c) measured. (d) simulated. (a-b) are far field element and (c-d) are near field element.

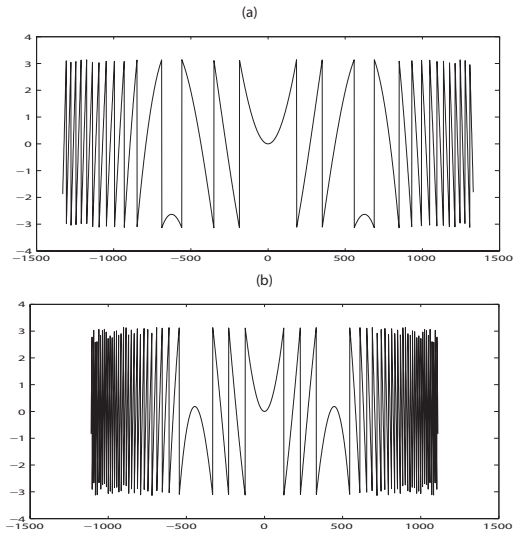

Figure 6.5: Improper sampling point in phase:(a) far-field.(b) Fresnel-domain. It can be seen that the effect of improper sampling is severe in Fresnel domain compared to far-field. Phase profile is no more continuous.

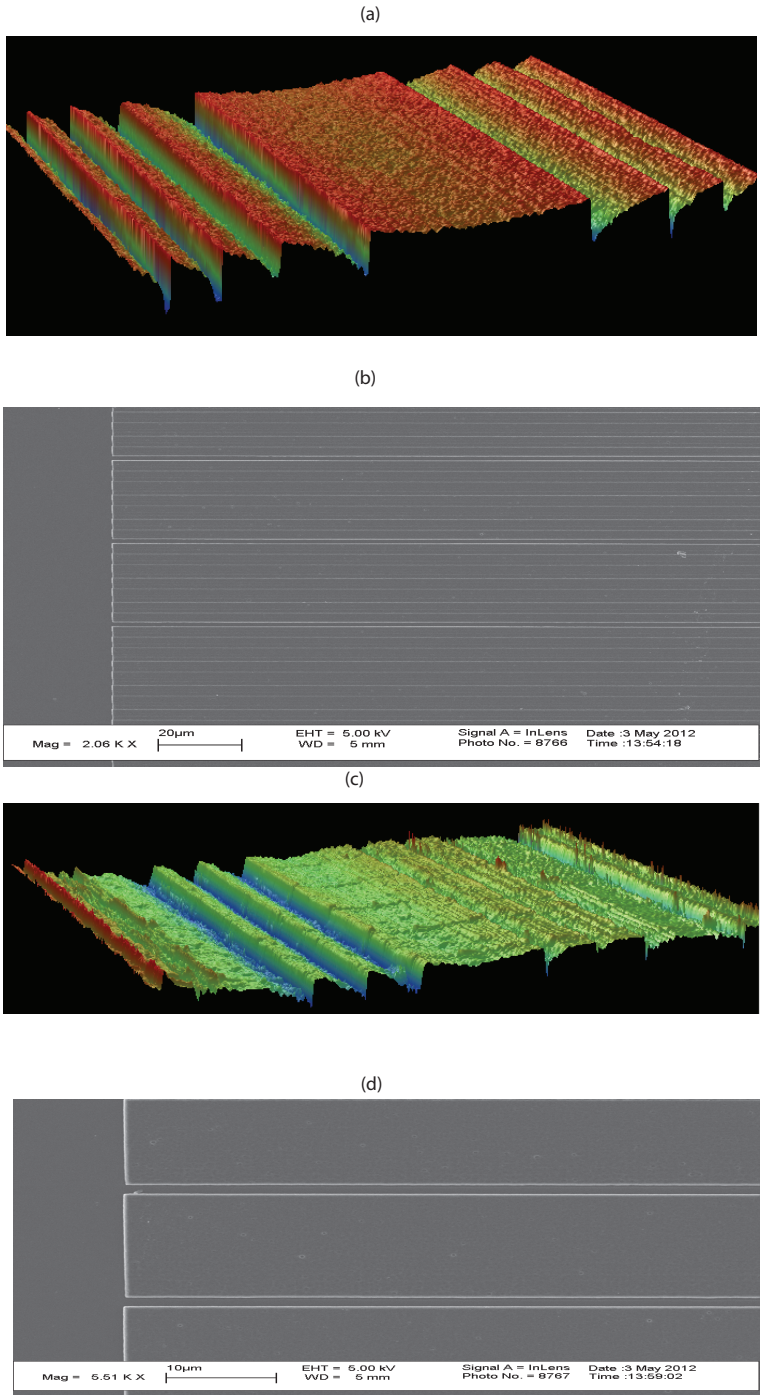

Figure 6.6: Phase profile:(a) 3-D image taken by optical profiler. (b) Top-view image take by SEM. (c) 3-D image taken by optical profiler.(d) Top-view image take by SEM. (a-b) are far field element and (c-d) are near field element.

6.2.1 Effect of etch depth error

Let us assume that we have an ideal phase function $\Phi(x)$. And this element has maximum height of the surface relief structure as t' instead of the design value t because of error in etch depth. Then we can define our transmission function as

$$t_x(x) = \exp[\mathrm{i}\alpha\Phi(\mathrm{x})] \tag{6.1}$$

where α is the ratio of fabricated height t' and designed height t and it doesn't change the periodicity of ideal phase function. Transmittance function can be elaborated by a generalized Fourier series expansion as [**?**]alpha)

$$t_x(x) = \sum_{m=-\infty}^{\infty} G_m \exp[\mathrm{i}m\Phi(\mathrm{x})], \tag{6.2}$$

where m is the diffraction order and coefficient G_m is

$$G_m = \frac{1}{2\pi}\int_0^{2\pi} \exp[\mathrm{i}(\alpha - m)\Phi(\mathrm{x})]\mathrm{d}\Phi(\mathrm{x}). \tag{6.3}$$

which gives

$$G_m = \mathrm{sinc}(\alpha - m)\exp[\mathrm{i}\pi(\alpha - m)]. \tag{6.4}$$

If $\alpha = 1$, then we can say that the wave is generated perfectly as generalized Fourier series contains only the first order term $m = 1$. But if $\alpha \neq 1$ then, there would be more of interference caused by generated noise fields and it would lead to loss of signal quality, and reduced diffraction efficiency.

There is another method for fabrication etch depth error analysis. The direct scaling technique can be described elegantly and generally as follows. If the ideal phase function of the DE is $\phi(x)$, we can generate its modulo 2π quantized version in the interval $[-\pi, \pi]$ using

$$\phi_{\mathrm{mod}}(x) = \arg\left\{\exp\left[\mathrm{i}\phi(x)\right]\right\}. \tag{6.5}$$

In case of scaling error described by a factor α, the phase function scaled to an internal $[-\alpha\pi, \alpha\pi]$ is $\alpha\phi_{\mathrm{mod}}(x)$ and the transmission function of the element is

$$t(x) = \exp\left[\mathrm{i}\alpha\phi_{\mathrm{mod}}(x)\right]. \tag{6.6}$$

This transmission function can be multiplied by the incident field the result can be used directly to propagate the output field into the target plane. The result is

then same as that given by the generalized order method when the number of orders included in the analysis is sufficiently large.

In order to explain it more explicitly, would apply the above mentioned analysis to triangular grating first as phase function of the elements designed in this thesis are similar to triangular grating and then to actual phase functions of the elements designed for this thesis. Phase function triangular grating is given in Eq.(6.7).

$$V_m(x, y) = \exp[-\mathrm{i}2\pi\mathrm{mx/d}] \tag{6.7}$$

The generalized orders are obtained by inserting the phase function into

$$V(x, y) = \sum_{m=-\infty}^{\infty} G_m V_m(x, y). \tag{6.8}$$

Here $V(x, y)$ is the field immediately after the element. Thus, different terms in Eq. (6.8) represent so-called generalized diffraction orders of the element, which have diffraction efficiencies as

$$\eta_m = \eta_m = |G_m|^2 . \tag{6.9}$$

Figure 6.7 shows the efficiency for diffraction orders -3 to 3 for different etch depth error (α).

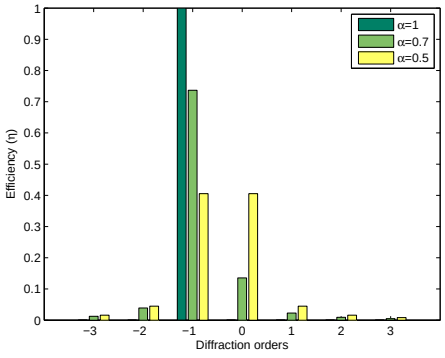

Figure 6.7: Efficiency of triangular grating for diffraction order -3 to 3 and α =1 is the case where wave is generated perfectly and as α decreases the interference increases as with simultaneously noise produced by other orders.

Now, inserting the phase function of far-field case , given by Eq. (**??**), we can use either of the above-described methods to analyze the effect of scaling errors in the quality of the flat-top profile. We can calculate the propagated field with actual fabrication etch depth error α= 0.7. It can be seen from Fig. 6.8(a)-Fig. 6.8(b) the results given by both methods are virtually similar.

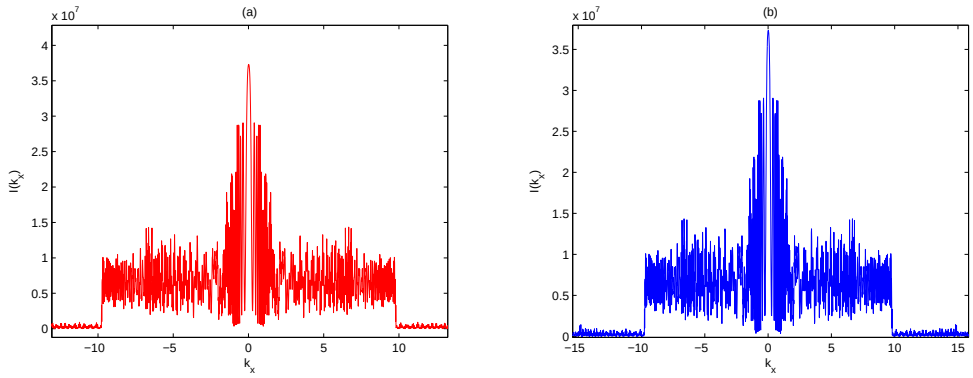

Figure 6.8: Far-field propagation:(a) Two π modulo method (b) Generalized-order approach

When $\alpha = 1$ there are no interference from the other diffraction orders but for case where $\alpha \neq 1$, there is many simultaneously generated noise fields . As the field from other orders overlap with $m = 1$, superposition of these fields is coherent which leads to reduced diffraction efficiency and non-uniform signal quality. Figures6.9 show the propagated field and the contribution of diffraction orders -2 to 2. Here zeroth order is similar to incident Gaussian beam and thus has a sharp central peak. The effect of -1^{st}, 2^{nd} and -2^{nd} orders is smaller compared to 0^{th} order.

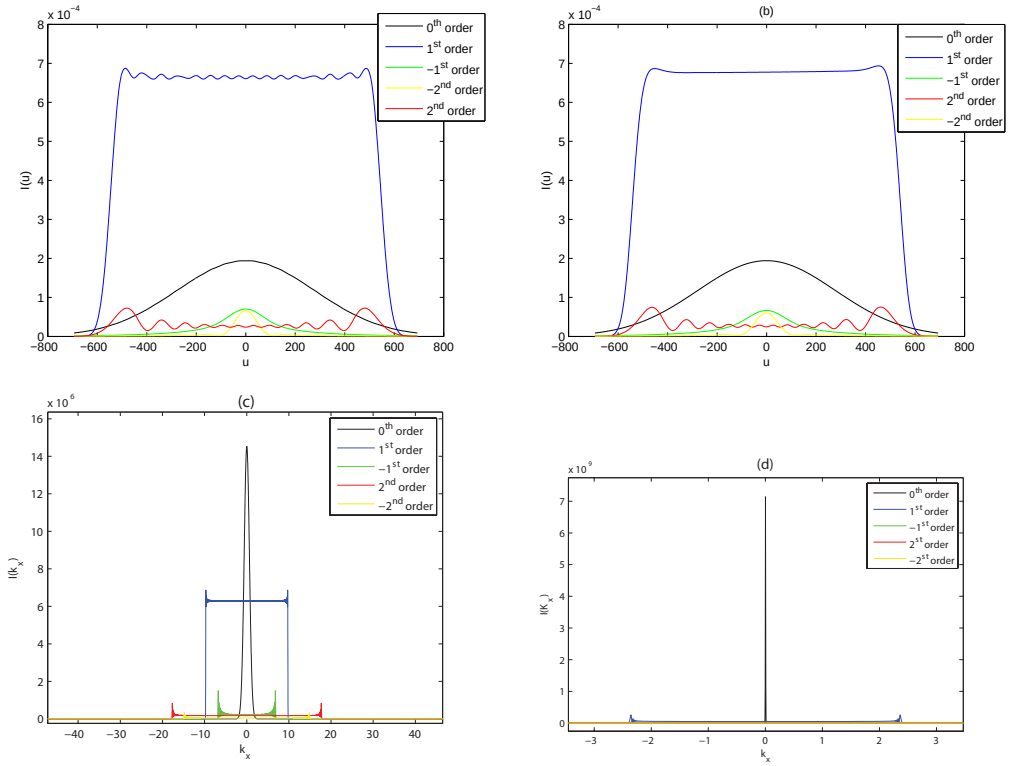

Figure 6.9: Propagated field(a) Fresnel domain element for exact flat top.(b) Fresnel domain element for super-Gaussian. (c) Far-field element for exact flat-top.(d) Far-field element for super-Gaussian. In (a)-(b)The etch depth error is α00.7 and is calculated for -3 to 3 diffraction orders

Effect of etch depth error is shown in Fig. 6.10. It can be seen from the figure that even small etch depth error produces a noisy field. Thus, all the phase function elements discussed in this thesis are very critical to phase depth error. To obtain high-quality flat-tops, only phase errors of a few per cent are allowed.

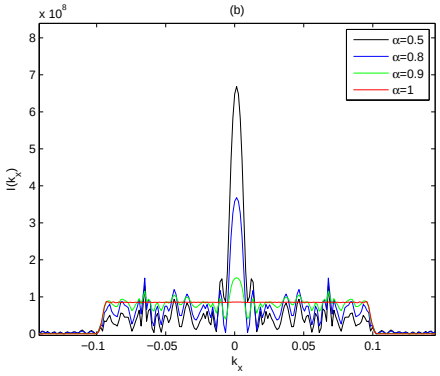

Figure 6.10: Transmitted far field beam for order -2 to 2 with different α.

6.3 Characterization

From Fig. 6.6 we can see that the phase profile of the elements is not perfect in these preliminary experiments. Thus, we cannot expect very good quality flat-tops or good results. Since there were so many different kinds of error it was difficult to calculate an accurate value of α. Thus, in experimental setup elements were adjusted so that best focus is obtained and then from simulation α was calculated such that the target intensity profile matched to that of experimental intensity profile.

6.3.1 Fresnel domain

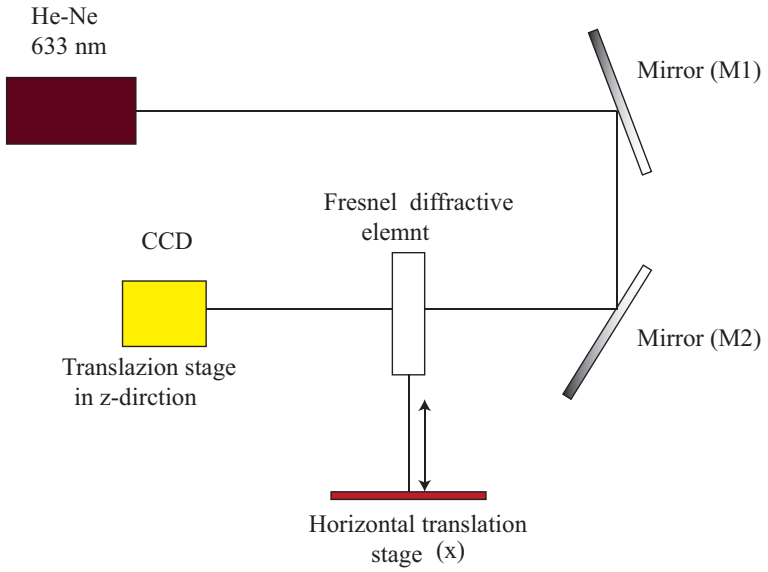

Figure 6.11: The setup employed in the experiment of Fresnel domain beam shaping.

Beam profiles were taken using beam profiler (WinCamD series). Input beam was He-Ne laser of 12 mW. Simulated and measured beam profile are shown below.

Fresnel domain:exact flat-top

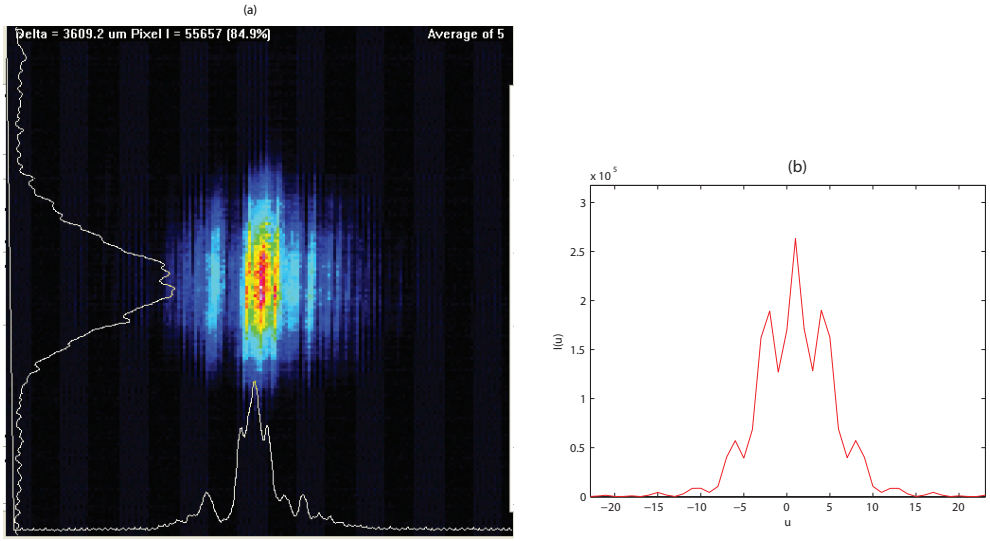

Figure 6.12: Target intensity profile (a) measured using beam profiler. Horizontal axis shows flat-top direction and vertical axis shows Gaussian beam direction. (b) simulated intensity profile with α=0.7.

From the figure we can see that the simulated result and the measured result are approximately similar. We could assume that if our element was perfect or had smaller error then it would have worked perfectly.

FRESNEL DOMAIN:SUPER-GAUSSIAN

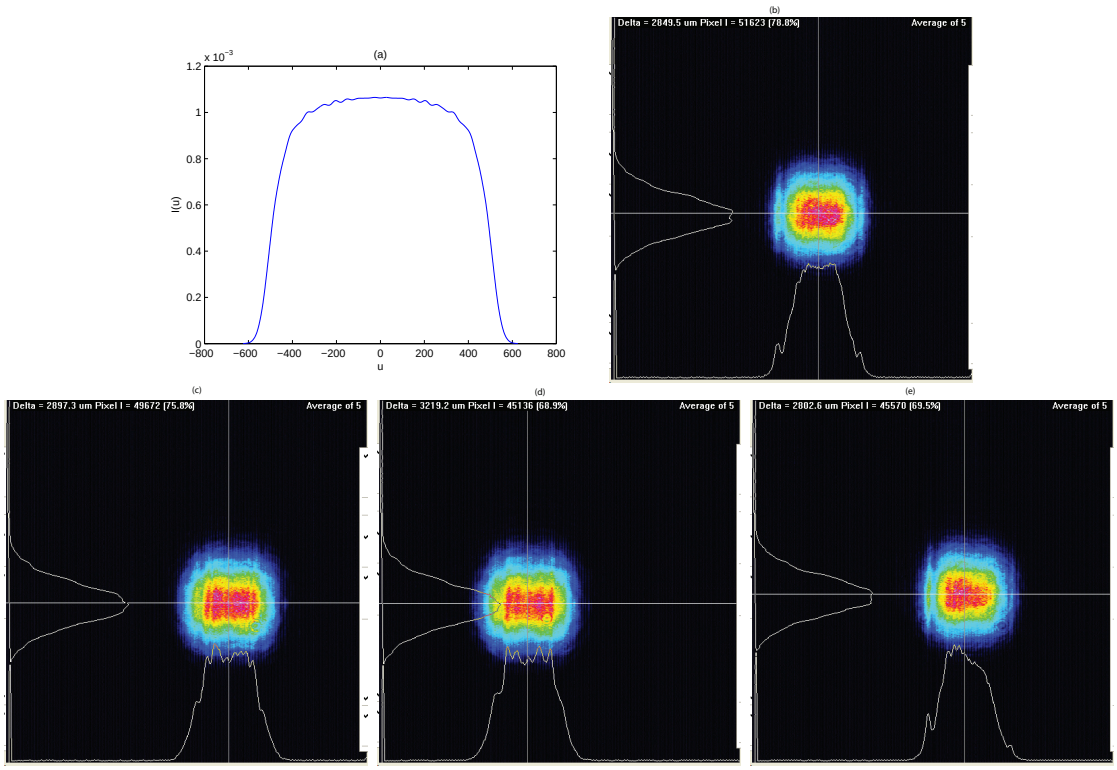

Figure 6.13: Target intensity profile (a) simulated intensity profile with α=0.84. (b) measured beam profile and correct position(longitudinally and laterally). (c) away from the correct position by 2 cm. (d) away from the correct position by 5 cm. (e) laterally displaced from correct position. In(b)-(e) target intensity is measured using beam profiler. Horizontal axis shows flat-top direction and vertical axis shows Gaussian beam direction.

For this element α is closer to 1 compared to other elements. Thus, we can see smoother flat-top and even the effect of lateral and longitudinal displacement is clearly visible. We can say that this element would have worked properly if error was in range of 5-10 percent.

6.3.2 Far-field

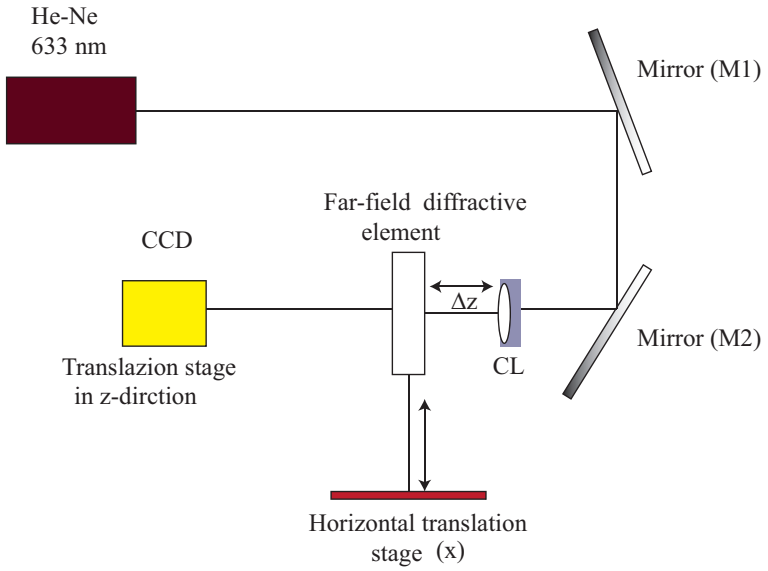

Figure 6.14: The setup employed in the experiment of Far-field beam shaping. Here CL is cylindrical lens.

Beam profiles were taken using beam profiler (WinCamD series). Again the beam was He-Ne laser of 12 mW. Simulated and measured beam profile are shown below.

FAR FIELD:EXACT

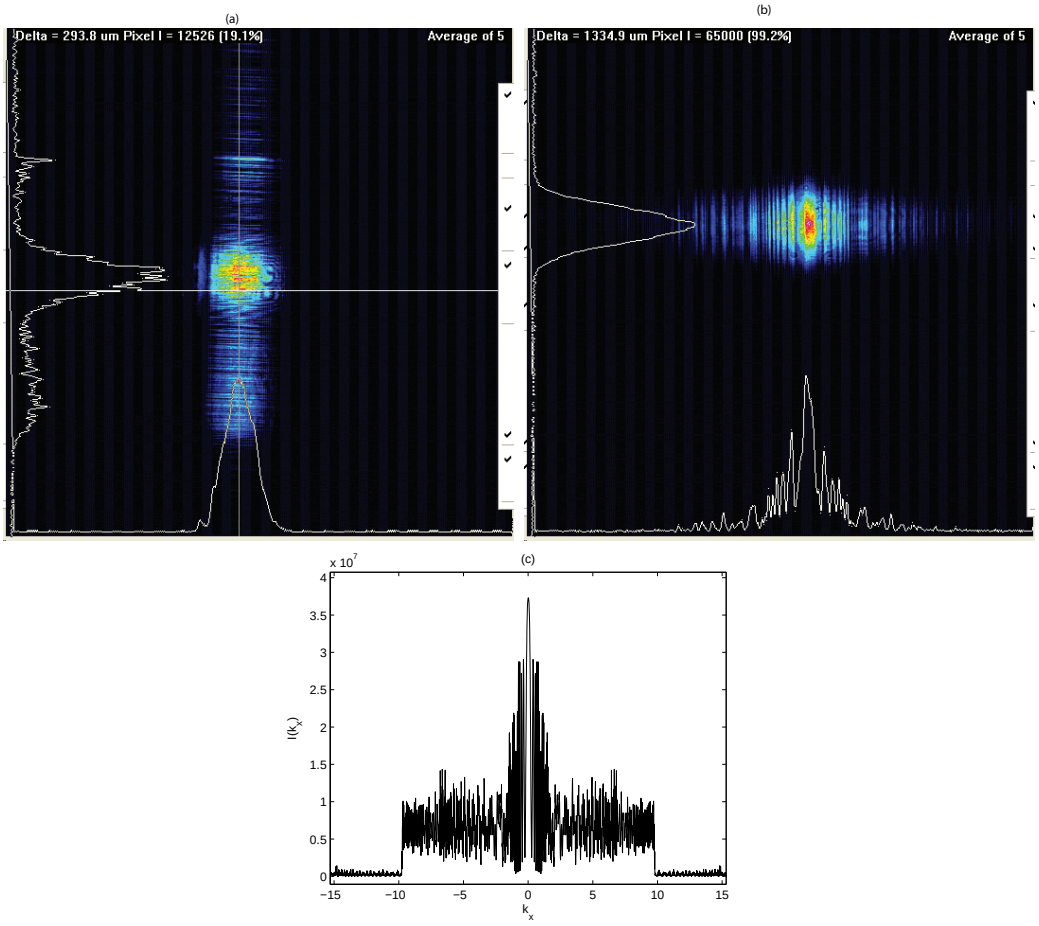

Figure 6.15: Target intensity profile (a) measured using beam profiler. Horizontal axis shows Gaussian beam direction and vertical axis shows flat-top direction. (b) measured using beam profiler. Horizontal axis shows flat-top direction and vertical axis shows Gaussian beam direction. (c) simulated intensity profile with α=0.7.

From the figure we can see that there is strong central peak with ripples through out the intensity profile and it is same for simulated and measured intensity distribution.

Far field:super-Gaussian

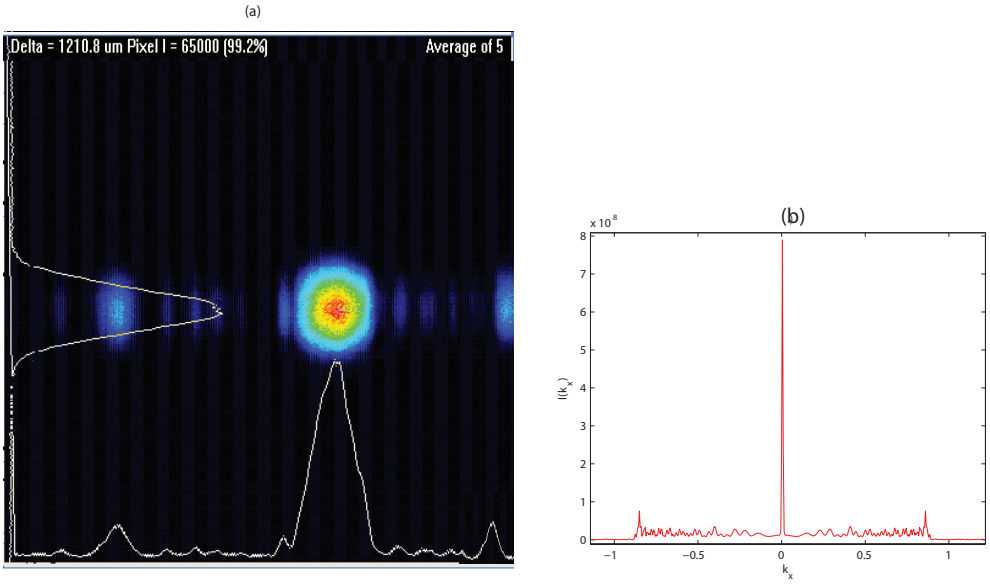

Figure 6.16: Target intensity profile (a) measured using beam profiler. Horizontal axis shows flat-top direction and vertical axis shows Gaussian beam direction. (b) simulated intensity profile with α=0.7.

From the measured figure we can see that the noise is comparatively higher than in the simulated intensity profile. The peaks in both corners of measured intensity profile are similar to that of simulated result. Central peak is strong in both measured and simulated results but the peak in measured result is much wider compared to that of simulation result.

Chapter VII

Conclusion

The diffractive beam shaping element is thin single element which can be installed easily in any optical setup. The beam shaping elements in this thesis are designed for Fresnel domain and far-field. Simulated results show that it possible to generate smooth flat-top with high efficiency and uniform intensity. Fresnel domain elements are critical about beam diameter, sometimes measured beam waist by CCD camera is not actual or real beam diameter as sometimes CCD camera are nonlinear. Then, we can let the laser beam propagate until the distance where the laser waist becomes accurate to design beam waist. For far-field case divergence angle is a critical issue we can compensate for variations in the divergence of the laser beam simply by adjusting the distance between the source and the element.

For both Fresnel and far-field case it was seen that positioning of the element was critical theoretically and experimentally. Transverse positioning errors were found to give non-symmetric profiles, it appeared that errors of beam waist w, longitudinal displacement(Δz), and divergence angle (Φ) lead to qualitatively similar effects: positive values $\Delta z > 0$ (distance between S and DE too large), an increase of Φ and w above there design values both lead to edge enhancement in the shaped profile. Correspondingly, negative values of Δz, as well as decrease in Φ and w give rise to rounding of the desired flat-top profile. Therefore we can compensate for variations in Φ and w simply by adjusting Δz slightly in the assembly phase of the setup in order to get a nice flat-top profile and use of high-order super-Gaussian target profiles.

The beam shaping element of present type had minimum local periods of $\sim 5\lambda$, and it was very difficult to fabricate highly efficient DEs. Thus, they suffered from

etch depth errors of 30 percent, which led to scattering of light into higher generalized orders of the DE. It was seen theoretically from simulated results and experimentally that the DE is very critical to profile height. As a result a wrong profile height led to generalized order producing high interference and reduced efficiency, thus leading asymmetry in the output profile. Use of diode pumped laser of wavelength $\sim$ 457 nm resulted in reduction of etch depth error by 5 percent. From simulated results it was found that the allowed error range was 2 percent but still this range can vary depending on application. Thus all output profiles showed a sharp central peak and it reduced with reduction in error.

At the time of writing this thesis, only few critical parameters were considered but many improvements and analysis are possible in future, as will be explained in chapter VIII.

Chapter VIII

Future-work

Beam shaping elements of present type have triangular local profile which have etch depth error and the triangular edges are rounded, which leads to scattering of light into higher generalized orders of the DE. Thus, in future more trial rounds in fabrication should be done to get the error in profile height small enough. Grating profiles with step or staircase form should be designed to reduce fabrication errors. Carrier grating in x direction should be used for designs with small divergence angle and carrier grating in y direction should be used for large angles to separate different diffraction orders, which will help in reducing interference caused by generalized orders and thus improving flat-top quality of our design.

Complex amplitude transmission approach was used to calculate the efficiency of different orders but in future rigorous diffraction theory like Fourier modal method (FMM) should be used in the analysis and design. FMM is a good approach for non paraxial cases like our case of focusing a laser beam on the grating with a cylindrical lens as it helps us to get refined structural parameters and accurate efficiency. One future goal is to design DE element for flat-top profile with supercontinum beams as the most of the spectral components experience a totally wrong phase delay like our present elements.

Bibliography

[1] F.M. Dickey and S.C. Holswade, Laser Beam Shaping: Theory and Techniques, *Mercel Dekker*, (2000).

[2] J. Turunen and F.Wyrowski, ed. , Diffractive Optics for Industrial and Commercial Applications, *Akademie Verlag*, Berlin, Germany, pp. 426 (1997).

[3] H. P. Herzig, ed., Micro-Optics: Elements, Systems And Applications, *Taylor and Francis*, London, 1997.

[4] W. Daschner, P. Long, R. Stein, C. Wu, and S. Lee, One step lithography for mass production of multilevel diffractive optical elements using high-energy beam sensitive (HEBS) grey-level mask, *Proc. SPIE*, **2689**, pp. 153-155 (1996).

[5] C. Hong-Wen, H. Ching-Ju, and L. Chung-Chi, Development of a novel optical CT employing a laser to create a collimated line-source with a flat-top intensity distribution, *Radiation Measurements*, **46**, pp. 1932-1935 (2011).

[6] M. F. Chen, K. M. Lin, and Y. S. Ho, Laser annealing process of ITO thin films using beam shaping technology, *Optics and Lasers in Engineering*, **50**, pp. 491-495 (2012).

[7] G. Raciukaitis, E. Stankevicius, P. Gecys, M. Gedvilas, C. Bischoff, E. Jaeger, U. Umhofer and F. Volklein, Laser processing by using diffractive optical laser beam shaping technique, *Journal of Laser Micro/Nanoengineering*, **6**, pp. 37-43 (2011).

[8] O. Homburg, D. Hauschild, F. Kubacki, and V. Lissotschenko, Efficient beam shaping for high-power laser applications. *Proc. SPIE*, **6216**, pp. 621-608 (2006).

[9] E. B. Kley, M. Cumme, L. C. Wittig, M. Thieme and W. Gabler, Beam shaping elements for holographic application, *Proc. SPIE*, **4179**, pp. 58 - 64 (2000).

[10] O. Bryndahl, Optical map transformation, *Opt. Commun.*, **10**, pp. 164-169 (1974).

[11] O. Bryndahl, Geometrical map transforms in optics, *J. Opt. Soc. Am.* **64**, pp. 1092-1099 (1974).

[12] C. N. Kurtz, H. O. Hoadley, and J. J. DePalma, Design and synthesis of random phase diffusers, *J.Opt.Soc.Am.*, **68**, pp. 1080-1092 (1973).

[13] B. Mercier, J.P. Rousseau, A. Jullien, and L. Antonucci, Nonlinear beam shaper for femtosecond laser pulses, from Gaussian to flat-top profile, *Opt. Commun.*, **283**, pp. 2900-2907 (2010).

[14] K. Sehun and O. Kyunghwan, 1D Bessel-like beam generation by highly directive transmission through a sub-wavelength slit embedded in periodic metallic grooves, *Optics Communications*, **284**, pp. 5388-5393 (2011).

[15] D. L. Shealy , J. A. Hoffnagle , Laser beam shaping profiles and propagation, *Applied Optics*, **45(21)**, pp. 5118-5131(2006).

[16] E. B. Kley, L. C. Wittig, M. Cumme, U. D. Zeitner, P. Dannberg, Fabrication and properties of refractive micro optical beam shaping elements, *SPIE*, **3879**, pp. 20-31(1999).

[17] Y. Xia, C. Ke-Qiu, and Z. Yan, Optimization design of diffractive phase elements for beam shaping, *Applied Optics*, **50**, pp. 5938-5943 (2011).

[18] B.R. Frieden, Lossless conversion of a plane laser wave to a plane wave of uniform irradiance, *Applied Optics*, **4**, pp. 1400-1403 (1965).

[19] C.Y. Han, Y. Ishii, and K. Murata, Reshaping collimated laser beams with Gaussian profile to uniform profiles, *Applied Optics*, **22**, pp. 3644-3647 (1983).

[20] J. Sochacki, A. Kolodziejczyk, Z. Jaroszewicz, and S. Bara, Nonparaxial design of generalized axicons, *Applied Optics*, **31(25)**, pp. 5326-5330 (1992).

[21] Z. Jaroszewicz, A. Kolodziejczyk, D. Mouriz, and J. Sochacki, Generalized zone plates focusing into arbitrary line segments, *Journal of Modern Optics*, **40 (4)**, pp. 601-612 (1993).

[22] Z. Jaroszewicz, J. Sochacki, A. Kolodziejczyk, and L. R. Staronski, Apodized annular-aperture logarithmic axicon:smoothness and uniformity of intensity distributions.*Optics Letters*, **18 (22)**, pp. 1893-1895 (1993).

[23] N. C. Roberts, Beam shaping by holographic filters. *Applied Optics*, **28 (1)**, pp. 31-32 (1989).

[24] M. A. Golub, I. N. Sisakyan, and V. A. Soifer, Infra-red Radiation Focusators, *Optics and Lasers in Engineering*, **15**, pp. 297-309 (1991).

[25] W. Singer, H. P. Herzig, M. Kuittinen, E. Piper, and J. Wangler, Diffractive beamshaping elements at the fabrication limit, *Optical Engineering*, **35 (10)**, pp. 2779-2787 (1996).

[26] H. Aagedal, M. Schmid, S. Egner, J. MÂÍuller-Quade, T. Beth, and F. Wyrowski, Analytical beam shaping with application to laser-diode arrays, *J. Opt. Soc. Am. A* , **14 (7)**, pp. 1549-1553 (1997).

[27] J. Jia, C. Zhou, X. Sun, and L. Liu, Superresolution laser beam shaping, *Applied Optics*, **43**, pp. 2112-2117 (2004).

[28] W. Mohammed and X. Gu, Long-period grating and its application in laser beam shaping in the 1:0m wavelength region, *Applied Optics*, **48**, pp. 2249-2254 (2009).

[29] R. Pereira, B. Weichelt, D. Liang, P. J. Morais, H. Gouveia, M. Abdou-Ahmed, A. Voss, and T. Graf, Efficient pump beam shaping for high-power thin-disk laser systems, *Applied Optics*, **49**, pp. 5157-5162 (2010).

[30] P. Laakkonen, M. Kuittinen, J. Simonen, and J. Turunen, Electron-beam-fabricated asymmetric transmission gratings for microspectroscopz, *Applied Optics*, **39**, pp. 3187-3191 (2000).

[31] J.C.Maxwell, Electricity and Magnetism, *Dover publication*, **chapter IX**, Vol.2, 3rd ed., New York, 1954.

[32] A. E. Siegman, Laser, *University Science Books*, **chapter XVII**, (1986).

[33] L. Mandel and E. Wolf, Optical Coherence and Quantum Optics, *Cambridge Univ. Press*, 1995.

[34] K. Knop, Rigorous diffraction theory for transmission phase grating with deep rectangular grooves, *J.Opt.Soc.Am*, **68**, pp. 1206-1210 (1978).

[35] J. Tervo, I. A. Turunen, and B. Bai, A general approach to the analysis and description of partially polarized light in rigorous grating theory, *Journal of the European Optical Society - Rapid publications*, **3**, 08004 pp. 1990-2573 (2008).

[36] C. Vieu, F. Carcenac, A. Pepin, Y.Chen, M. Mejias, A. Lebib, L. Manin-Ferlazzo, L. Couraud, and H. Launois, Electron beam lithography: resolution limits and applications, *Appl. Surf. Sci.*, **164**, pp. 111-117 (2000).

[37] P. Zhou, and J. H. Burge , Fabrication error analysis and experimental demonstration for computer-generated holograms, *Applied Optics*, **46** (5), pp. 657-663 (2007).

[38] P. Ehbets, M. Rossi, and P. H. Herzig, Continuous-relief fan-out elements with optimized fabrication tolerances, *Optical Engineering* **34(12)**, pp. 3456-3464, (1995)